

High-Resolution Non-Invasive X-ray Diffraction Analysis of Artists' Paints: Supplementary Material

1. Test Panel



Fig. S1. Photograph of the panel of test paints. An EDXRD spectrum of the paint on the canvas was also acquired – this paint contains the titanium white pigment (TiO_2 , rutile).

Table S1. Grid showing the identification of each paint (supplier's name), matching the layout in Fig. S1.

Cerulean Blue	Cobalt Blue	Phthalocyanine Blue Lake	Manganese Blue	Ultramarine Blue	Dioxazine Violet	Manganese Violet
Terre Vert	Chrome Oxide Green	Cobalt Turquoise	Phthalocyanine Green Lake	Viridian	Chrome Green	
Lemon Yellow	Bright Yellow Lake	Aureolin	Yellow Lake	Naples Yellow	Cadmium Gold Yellow	Chrome Yellow
Vermilion	Minium	Orange Molybdate	Pyrrolo Vermilion	Naphthol Red	Scarlet Lake	Cadmium Red
Alizarin Crimson	Magenta	French Yellow Ochre	Raw Sienna	Raw Umber	Transparent Oxide Red	
Cremnitz White	Flake White	Barite White	Zinc White	Flemish White	Titanium White No. 3	
Ivory Black	Lamp Black					

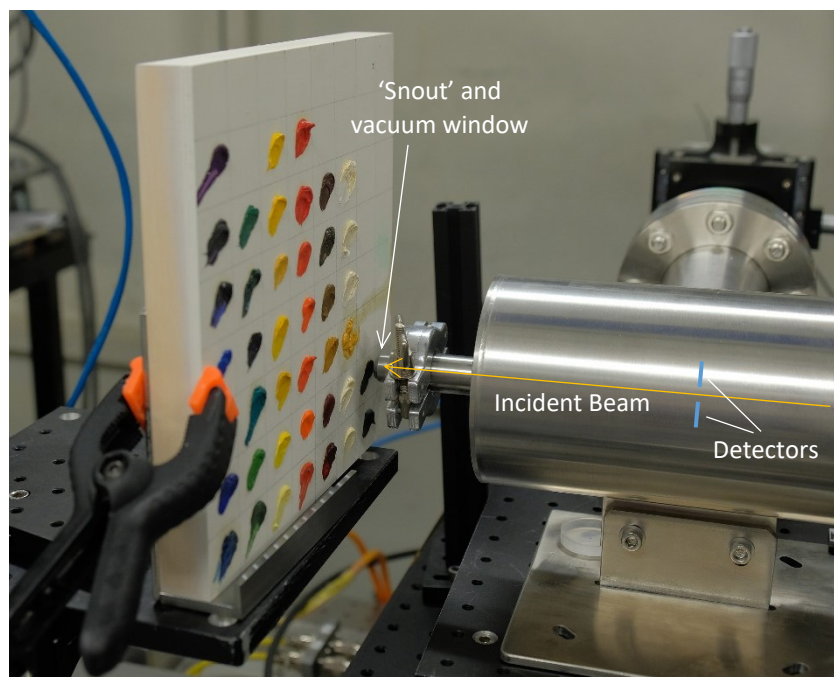


Fig. S2. Photograph of the test panel mounted in position for a measurement. The panel was secured on an xyz -translation stage and positioned so that each paint was within 2 – 3 mm of the vacuum window at the end of the ‘snout’. The location of the detectors within the vacuum chamber is indicated on the photograph (not to scale).

2. Calibration of the February 2019 Data

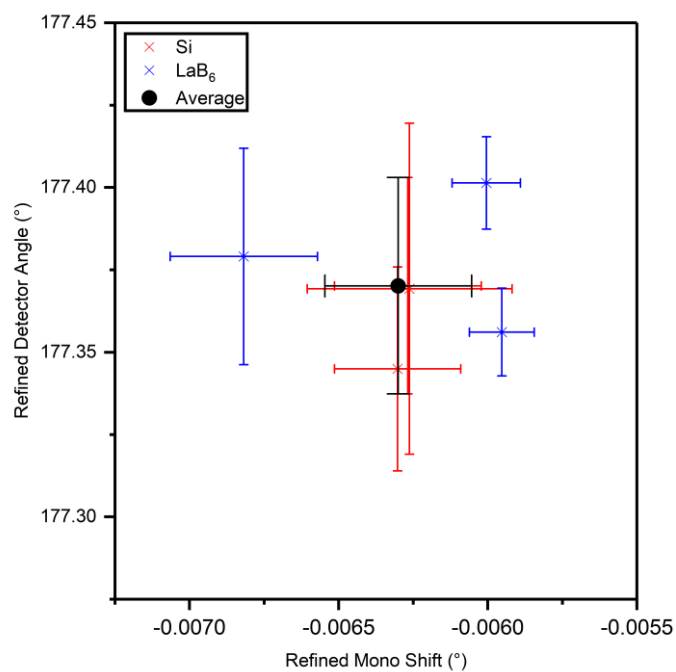


Fig. S3. Calibration of $\delta\theta$ and $\delta\theta_{\text{DCM}}$ using the LaB₆ and Si powder SRMs for the February 2019 beamtime data (see Section 2.3.1 of the main article).

3. Validation of Phase Quantification

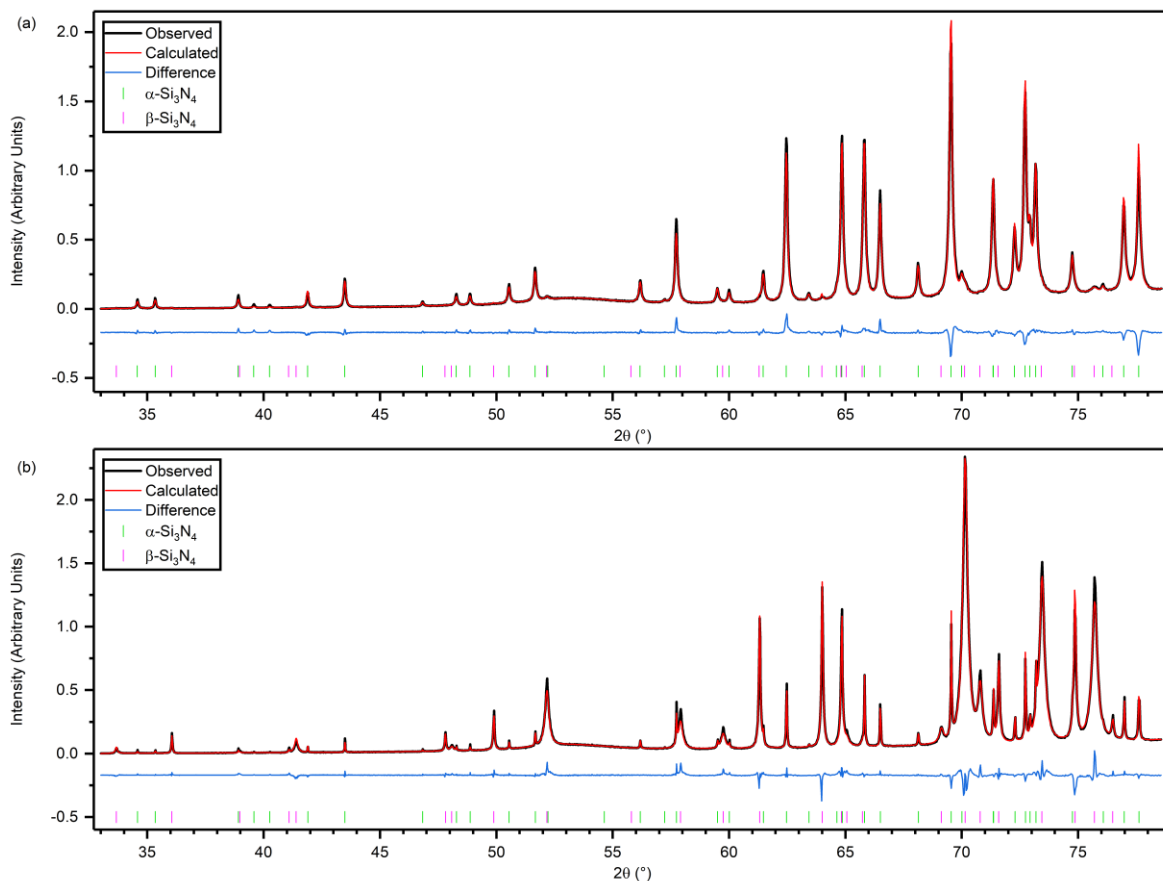


Fig. S4. Rietveld refinements of the NIST 656 SRM data: (a) α 656, (b) β 656.

Table S2. Comparison of the NIST certified quantification of α - and β - Si_3N_4 in SRM 656 with fitted values in this work.

Standard	NIST Certification*	Rietveld Fit
α 656		
α (%)	96.7 (1)	97.0 (2)
β (%)	3.3 (1)	3.0 (2)
b^\dagger		3.37 (3)
R_{wp} (%)		6.55
β 656		
α (%)	17.8 (3)	13.3 (7)
β (%)	82.2 (3)	86.7 (7)
b^\dagger		3.59 (2)
R_{wp} (%)		7.50

*The NIST quantification includes amorphous content. The crystalline component quantities have been normalised to 100% in this table.

† Parameter from the $a\theta^b$ scaling factor. The a parameter is the overall linear scaling parameter with arbitrary units.

The Rietveld refinements of the NIST 656 SRM data acquired during the January 2020 beamtime are shown in Fig. S4 and the quantitative results are reported in Table S2. The values for the α 656 component agree within errors while there is a discrepancy of 4.5% in the quantification of β 656. The powder averaging for both components is good but is somewhat worse for β 656 and this factor provides

a possible explanation for the error in quantification. It is also possible that the $a\theta^b$ scaling factor is failing to accurately account for the intensity variation as a function of X-ray energy. The magnitude of the discrepancy provides a rough estimate of the likely uncertainties in the phase quantifications of the paint samples.

4. Assessment of Powder Averaging

As described in Sections 2.2 and 3 of the main article, the degree of powder averaging can be assessed qualitatively by comparison of the diffraction peak intensities in each of the detector channels (two working detectors in the February 2019 beamtime and four in January 2020). The figures below (S4 – S7) illustrate the behaviour ranging from good powder averaging to poor. Naturally, the assessment is better with four available detectors and all the examples have been chosen from the January 2020 beamtime.

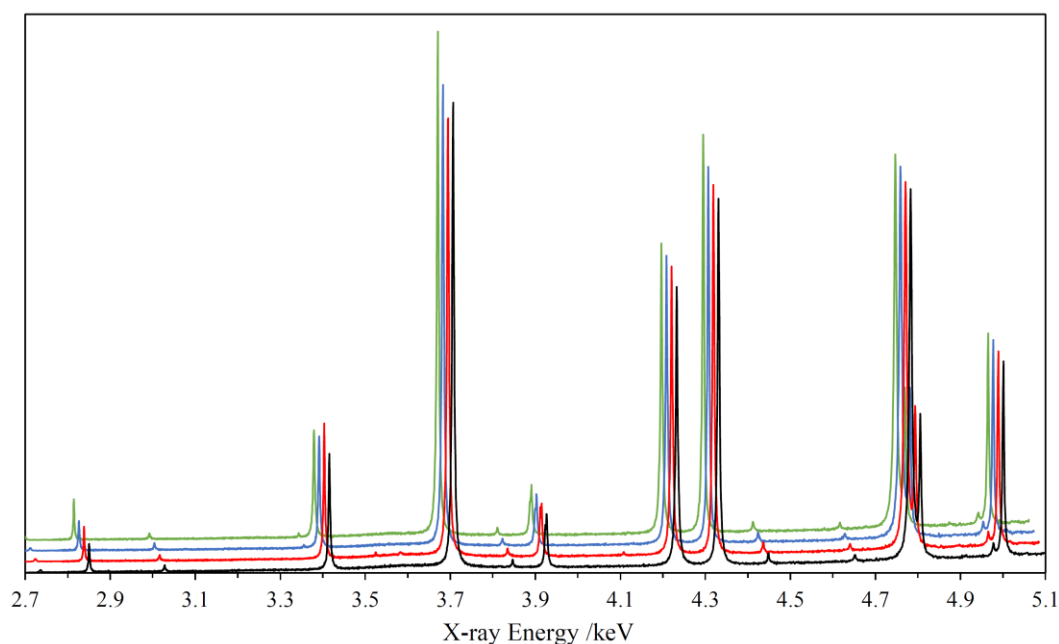


Fig. S5. EDXRD data for the Chrome Oxide Green paint illustrating relatively good powder averaging. The four detector channels have been offset relative to each other on both axes to allow easier comparison. Although the diffraction peak intensities are very similar in all four channels, some differences are apparent e.g. the most intense peak near 3.7 keV.

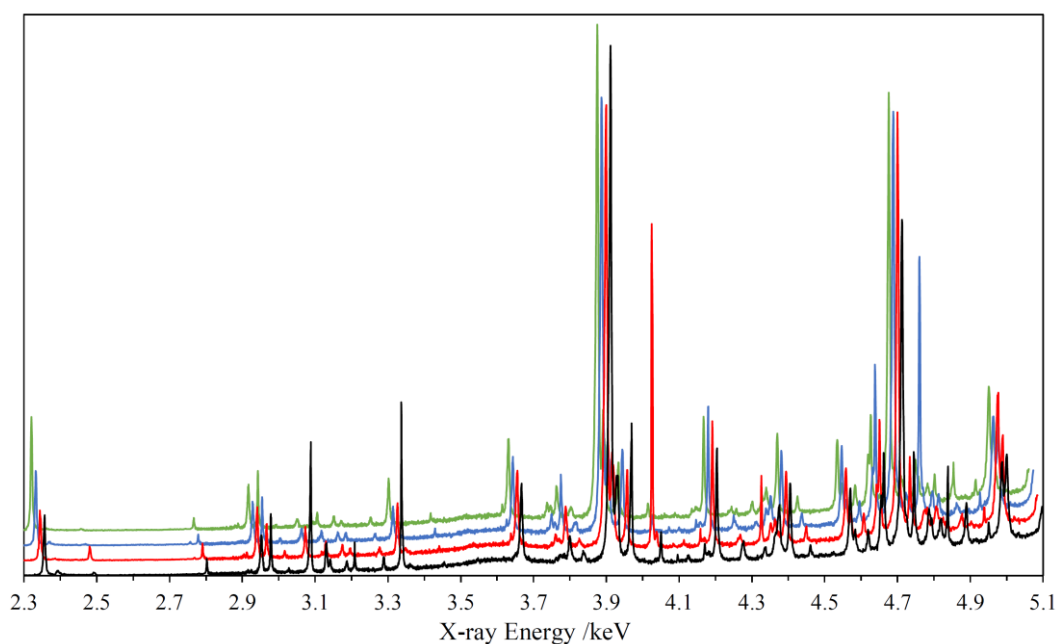


Fig. S6. EDXRD data for the Cremnitz White paint illustrating moderately good powder averaging ('intermediate behaviour'). The four detector channels have been offset relative to each other on both axes to allow easier comparison. Virtually all the diffraction peaks are present in all four channels, but with significant variations in intensity in some instances.

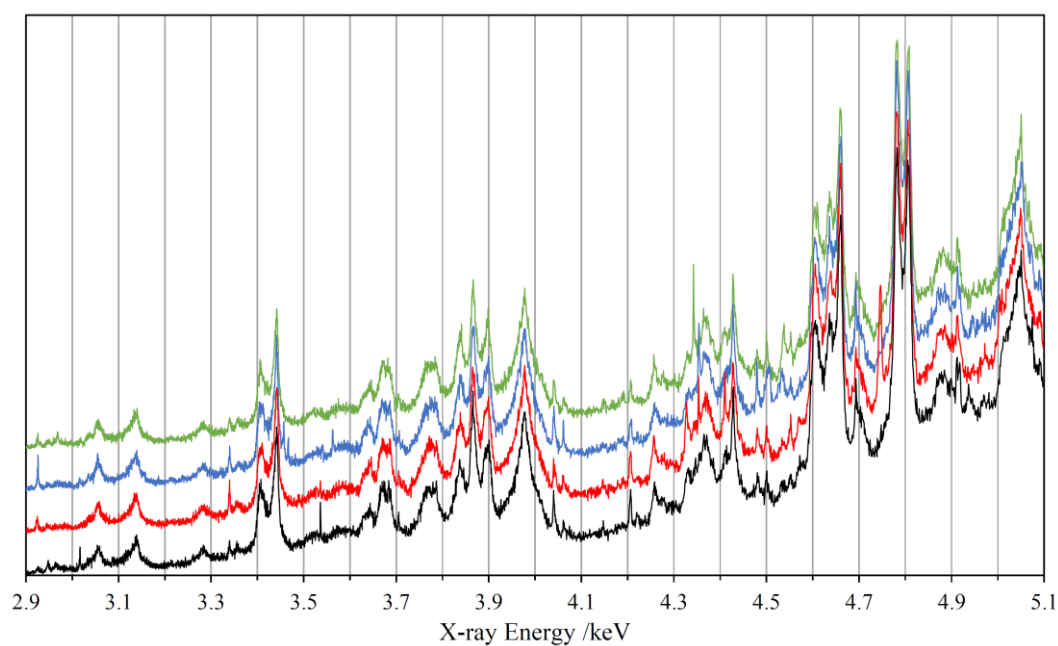


Fig. S7. EDXRD data for the Orange Molybdate paint illustrating variable powder averaging. The four detector channels have been offset relative to each other on the vertical axis to allow easier comparison. The broad diffraction peaks have very similar intensities in all four channels while there are a number of sharp peaks that appear on just one channel. The most obvious interpretation is the presence of (at least) two crystalline phases, one with small crystallites leading to good powder averaging and size-broadening of peaks, and the other with relatively large crystallites leading to poor powder averaging but very sharp peaks.

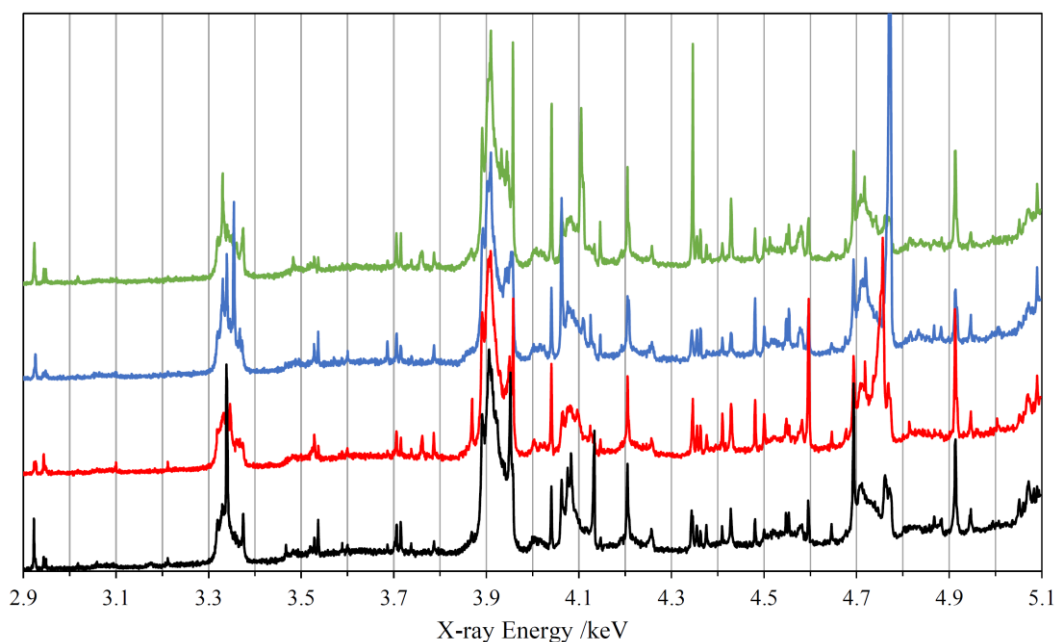


Fig. S8. EDXRD data for the Naples Yellow paint illustrating variable powder averaging. The four detector channels have been offset relative to each other on the vertical axis to allow easier comparison. Some diffraction peaks have very similar intensities in all four channels while others vary significantly.

5. X-ray Penetration Depth

The penetration depth of X-rays into a material depends strongly on the X-ray energy (as well as the material composition and density). Fig. S9 shows the penetration depth of X-rays into a triglyceride (formula $C_{55}H_{98}O_6$, density 0.93 g cm^{-3}) representing an oil-based medium such as linseed oil. The depth shown is half of the $1/e$ attenuation length in order to represent the depth at which X-ray photons can interact (diffract) and then re-emerge from the material with total $1/e$ attenuation. It is important to note that the presence of other materials within the oil, such as pigments and fillers, will in most cases significantly reduce the penetration depth. The $1/e$ attenuation length was calculated using the Center for X-ray Optics online calculator (https://henke.lbl.gov/optical_constants/).

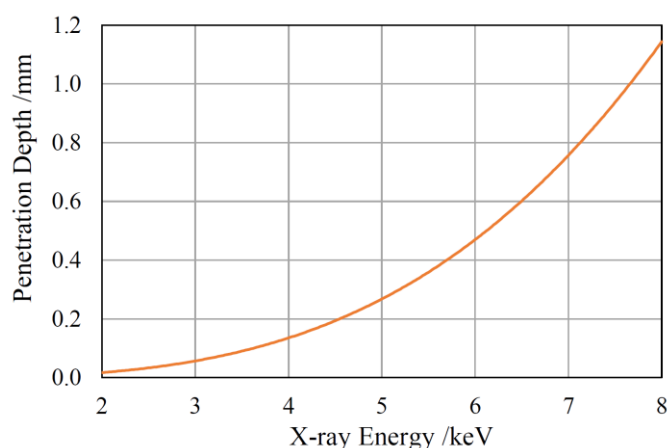


Fig. S9. Penetration depth of X-rays into a typical oil medium. See the main text for full details.

6. Comparison with Laboratory XRD

To place the performance of the back-reflection EDXRD technique in context, the results should ideally be compared with the results of another non-invasive XRD method using either portable or laboratory-based instrumentation. Unfortunately, the authors do not have access to an instrument of this type. Instead, data for two of the paints (Cobalt Blue and Cremnitz White) were acquired using a conventional laboratory XRD instrument. Small samples of the paints, on the order of a few mg, were removed from the test panel using a sharp scalpel. The Cremnitz White sample was ground to a powder by hand using a pestle and mortar but this method was ineffective for the Cobalt Blue sample which was finely diced with a razor blade instead. Each sample was sprinkled onto a low background silicon wafer and calibration was provided by the NIST Si standard (SRM 640a), also on a low background holder. In each case, the holder was spun at 15 rpm during data acquisition to improve powder averaging. Data was acquired with a Bruker D8 Advance using Cu-K α radiation and a Ni filter. The incident and diffracted beams were both collimated with 2.5° Soller slits and a Lynxeye XE position sensitive detector was used. Using the Si standard data, the instrumental FWHM resolution is 0.102° and 0.111° at 30° and 70°2 θ respectively.

Direct comparisons of the laboratory and synchrotron data are shown in Figs S10 and S11 for Cobalt Blue and Cremnitz White respectively. The synchrotron EDXRD data has been converted to the angular equivalent using a wavelength of 1.5406 Å. There are small relative shifts in the diffraction peak positions because of sample height errors in the laboratory data. The synchrotron data has been scaled using a smooth, variable function to allow easier comparison of each observed diffraction peak, and the vertical axes are meaningful in terms of counts only for the laboratory data. The Si standard data is also shown in Fig. S10. The very sharp peaks seen in the synchrotron data is due to a small amount of corundum in the paint, unfortunately below the detection limit in the laboratory data. However, it is instructive to visually compare the synchrotron corundum peaks with the laboratory Si peaks as, in each case, the peak widths are dominated by the instrumental contribution with negligible sample contribution. The remaining peaks are due to the cobalt aluminate (CoAl₂O₄) pigment and are clearly broadened in both datasets.

Fig. S11 shows the same direct comparison for the Cremnitz White paint. Considerable differences in the relative peak intensities are apparent between the laboratory and synchrotron data. A Rietveld fit to the laboratory data shows that although the hydrocerussite phase shows preferred orientation (of the 00/ planes parallel to the sample surface), the strength of the effect is significantly smaller. As a consequence of the sample preparation method for the lab data, there is no reason to expect this parameter to remain the same and indeed this represents a loss of information relative to the undisturbed paint on the test panel. A second difference is that the Rietveld fit to the laboratory data shows a cerussite content of 31 wt% in the two-phase mixture, compared to 19 wt% derived from the synchrotron data. The powder averaging is significantly better in the laboratory data and it is likely that the poorer powder averaging adversely affects the quantification accuracy of the synchrotron data. The resolution of the laboratory data was insufficient to support an analysis of the anisotropic crystallite shape model fitted to the synchrotron data.

It is not surprising that the quality of the synchrotron data, particularly regarding instrumental resolution and signal-to-noise ratios, is superior. However, it is emphasised that the authors plan to implement the back-reflection EDXRD technique in the laboratory using microcalorimeter technology which is expected to lead to only a modest loss of resolution and comparable signal-to-noise for the same acquisition times (because of the broadband acquisition advantage). The synchrotron data is therefore representative of the expected performance of laboratory back-reflection EDXRD.

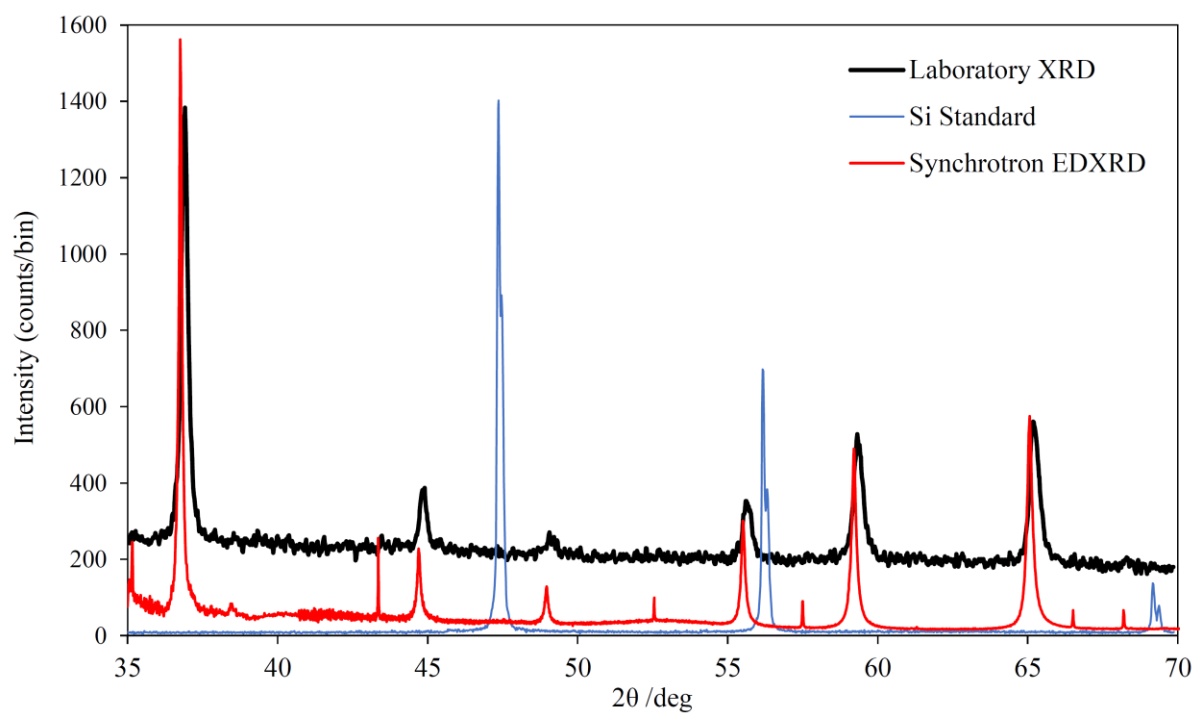


Fig. S10. Comparison of laboratory and synchrotron XRD data for the Cobalt Blue paint. The NIST Si standard laboratory data is also shown (scaled by a factor of 0.2 relative to the Cobalt Blue pattern).

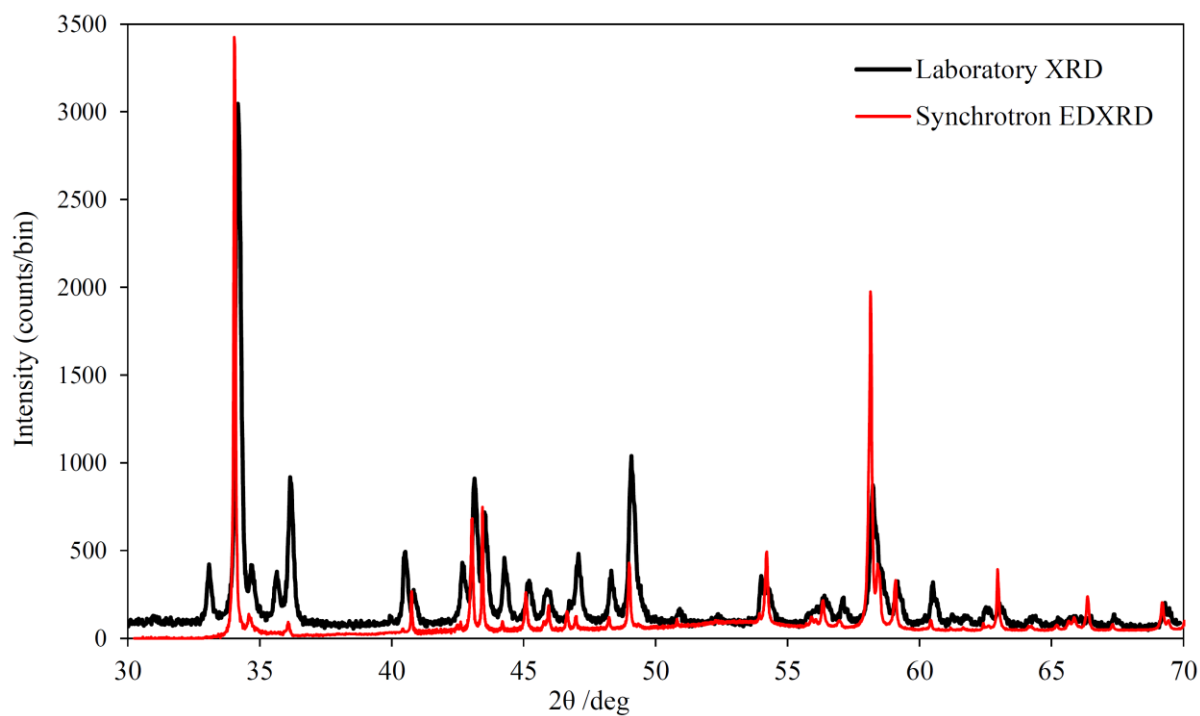


Fig. S11. Comparison of laboratory and synchrotron XRD data for the Cremnitz White paint.

7. Artists' Paints

This section reports the results for the paints not described in the Results section of the main article. The paints have been categorised into four groups A – D, defined in Section 3 of the main article (Table S3). The diffraction patterns are shown along with Pawley fits and Rietveld refinements if an analysis was possible. For all of these paints, the diffraction peaks are broadened by sample effects i.e. the peaks are broader than the observed diffraction peaks of the LaB₆ standard for which the broadening is instrumental (primarily geometrical). In most cases no attempt has been made to distinguish between the most common causes of peak broadening – small crystallite mean size and microstrain. Except where otherwise noted, size broadening effects have been assumed whenever the broadening appears to be isotropic (with no *hkl* dependence). The reported crystallite domain sizes should be interpreted in this context. The same approach has been taken even for phases that exhibit poor powder averaging despite the fact that this observation implies the presence of larger crystallites.

For some of the diffraction patterns, absorption edge jumps and the associated EXAFS pattern have been subtracted from the data using a simple algorithm that takes account of the overlap between the ‘moving window’ [1] and the K β fluorescence peak corresponding to the element responsible for the absorption edge. The intensity of the K β peak at each monochromator energy was estimated by scaling the observed K α peak intensity (the K α peak is fully resolved from the scattered/diffracted monochromator energy by the SDDs, unlike the K β peak). This method has been implemented only for K-edges.

Table S3. Panel paints categorised into groups A – D.

Group A		Group B	Group C	Group D
Cerulean Blue	Minium	Manganese Blue	Terre Vert	Phthalo Blue Lake
Cobalt Blue	Cadmium Red	Dioxazine Violet	Orange Molybdate	Phthalo Green Lake
Ultramarine Blue	French Yellow Ochre	Bright Yellow Lake	Viridian	Yellow Lake
Manganese Violet	Raw Sienna	Pyrrolo Vermilion		Naphthol Red
Chrome Oxide Green	Raw Umber			Scarlet Lake
Cobalt Turquoise	Transparent Red Oxide			Alizarin Crimson
Chrome Green	Cremnitz White			Magenta
Lemon Yellow	Flake White			Lamp Black
Aureolin	Zinc White			
Naples Yellow	Flemish White			
Cadmium Gold Yellow	Titanium White No. 3			
Chrome Yellow	Ivory Black ^a			
Vermilion				

^aThe black pigment in this paint is expected to be carbonaceous material which has not been detected (detection of the pigment is the definition for group A paints). However, the pigmentation is derived from charred animal bones and hydroxyapatite has been detected; this mineral is intimately associated with the pigment, justifying categorisation in group A.

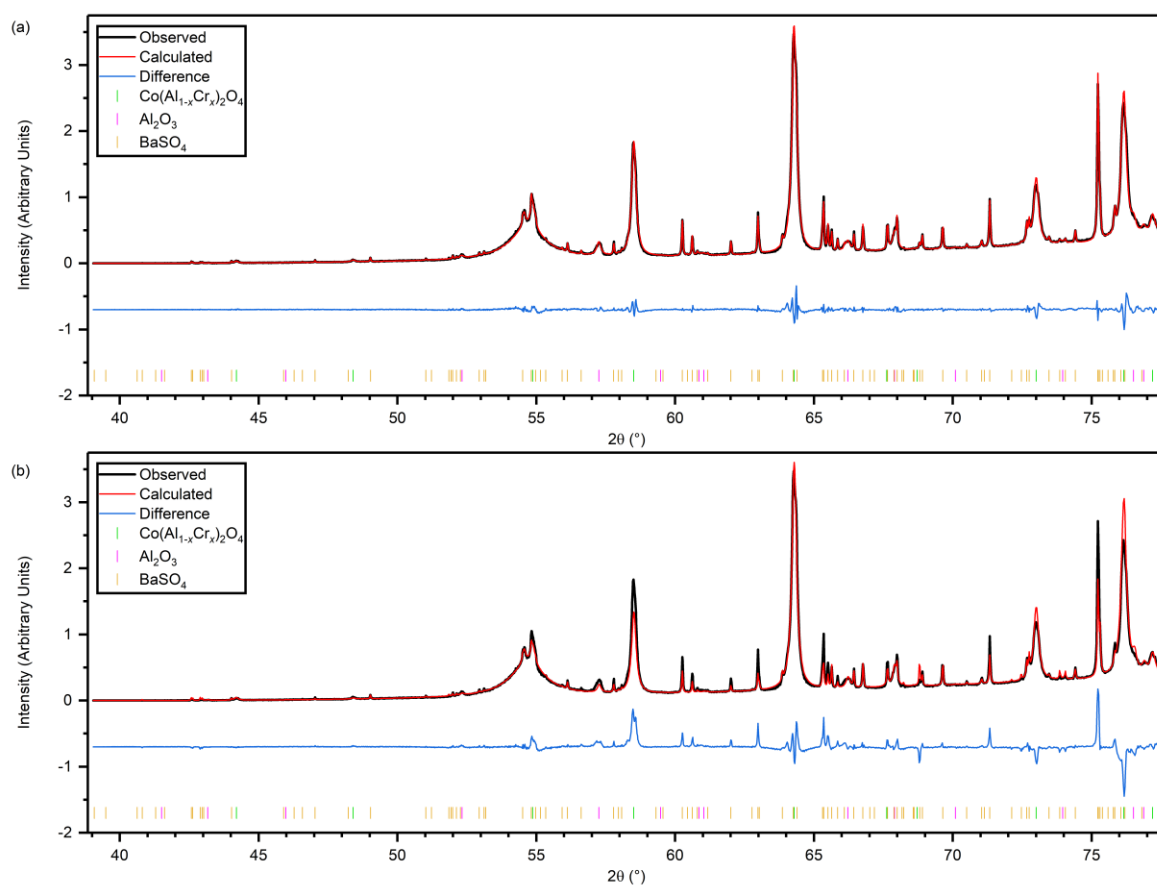
7.1 Group A Paints

Cerulean Blue (Michael Harding No. 603)

The strongest diffraction peaks were readily fitted by those of a spinel with all remaining peaks attributed to Al₂O₃ and BaSO₄ (Fig. S10a). The spinel is presumed to have nominal formula Co(Al_{1-x}Cr_x)₂O₄, based on previous elemental and Raman analysis of the paint [2]. A Rietveld refinement was carried out to determine phase fractions (Fig. S10b, Table S4); the two detectors exhibited different intensities for the BaSO₄ peaks and so phase quantification error is likely larger than the estimated standard uncertainty quoted. In order to determine the extent of Cr substitution in the spinel phase from the XRD pattern, two analytical approaches can be taken:

Table S4. Refined crystallographic parameters for the identified phases in Cerulean Blue.

	Literature	Pawley Fit	Rietveld Fit
Co(Al_{1-x}Cr_x)₂O₄ (<i>Fd</i>$\bar{3}$<i>m</i>)	ICSD Code 78402 ^a		
<i>a</i> (Å)	8.10664 (4)	8.18999 (5)	8.18974 (9)
Crystallite size (nm)		36.3 (2)	35.2 (4)
<i>x</i>		0.37 ^b	0.214 (15)
Weight fraction (%)			82.2 (6)
Al₂O₃ (<i>R</i>$\bar{3}$<i>c</i>)	ICSD Code 51687		
<i>a</i> (Å)	4.7597 (1)	4.7779 (2)	4.7774 (3)
<i>c</i> (Å)	12.9935 (3)	13.0440 (8)	13.0385 (16)
Crystallite size (nm)		37.3 (12)	45 (3)
Weight fraction (%)			10.3 (5)
BaSO₄ (<i>Pnma</i>)	ICSD Code 200112		
<i>a</i> (Å)	8.8842 (12)	8.87491 (7)	8.87465 (19)
<i>b</i> (Å)	5.4559 (8)	5.45321 (5)	5.45351 (9)
<i>c</i> (Å)	7.1569 (9)	7.15351 (5)	7.15341 (16)
Crystallite size (nm)		222 (4)	247 (13)
Weight fraction (%)			7.6 ^c (3)
<i>R</i> _{wp} (%)		6.08	14.8

^aCoAl₂O₄.^bInferred from Vegard's Law, see text.^cThis phase has poor powder averaging.**Fig. S12.** (a) Pawley and (b) Rietveld fits to the Cerulean Blue diffraction pattern. In each case the difference plot is shown offset on the vertical scale. The broad peak centred on $2\theta = 54.8^\circ$ is due to diffraction by the graphitic vacuum window, and was fitted by inclusion of two pseudo-Voigt functions.

1. Vegard's Law

The value of x can be inferred from the lattice parameter using Vegard's law. Only the end-members, CoAl_2O_4 and CoCr_2O_4 , are available on the ICSD (Codes 78402 and 61612, respectively) with lattice parameters 8.10664 (4) Å and 8.3346 (3) Å, respectively. Based on the lattice parameter extracted from the Pawley fit of 8.18999 (5) Å (Table S4), x can be interpolated as 0.37 (1) (the error estimate is based only on prior experience of accuracy using lattice parameter interpolation).

2. Site Occupancy Refinement

As part of the Rietveld fit, the relative occupancy of the (Al,Cr) 16d site can be refined. The total occupancy was constrained to unity and x refined to 0.214 (15). All other crystallographic parameters (O coordinates, atomic displacement parameters) remained fixed at the values obtained from the ICSD Code 78402 crystal structure.

The values of x obtained from the two approaches are significantly different and both have assumptions that limit the reliability of these analyses. The former assumes that the solid solution obeys Vegard's law (i.e. linearity of lattice parameters vs x), whilst the latter assumes that there is no preferred orientation of the crystallites. Both approaches assume that Cr is the only significant substituent in the spinel and that the crystal structure is otherwise unchanged. On the basis that Vegard's law is accurately obeyed for related spinels [e.g. $\text{Zn}(\text{Al}_{1-x}\text{Cr}_x)_2\text{O}_4$, see ref. 3], it is believed that the estimate of x based on lattice parameter interpolation is more reliable.

It is noted that the refined unit cell parameters of Al_2O_3 show a slightly enlarged cell, possibly due to Co or Cr substitution into the corundum structure, but no attempt was made to quantify this.

Cobalt Blue (Michael Harding No. 506)

Table S5. Refined crystallographic parameters for the identified phases in Cobalt Blue.

	Literature	Pawley Fit	Rietveld Fit
CoAl_2O_4 ($Fd\bar{3}m$)	ICSD Code 78402		
a (Å)	8.10664 (4)	8.10236 (2)	8.10238 (2)
Crystallite size (nm)		33.14 (8)	33.65 (11)
Weight fraction (%)			96.91 (10)
Al_2O_3 ($R\bar{3}c$)	ICSD Code 51687		
a (Å)	4.7597 (1)	4.75945 (3)	4.75944 (4)
c (Å)	12.9935 (3)	12.99219 (12)	12.99213 (18)
Crystallite size (nm)		291 (13)	280 (20)
Weight fraction (%)			3.09 (10)
R_{wp} (%)		6.16	8.32

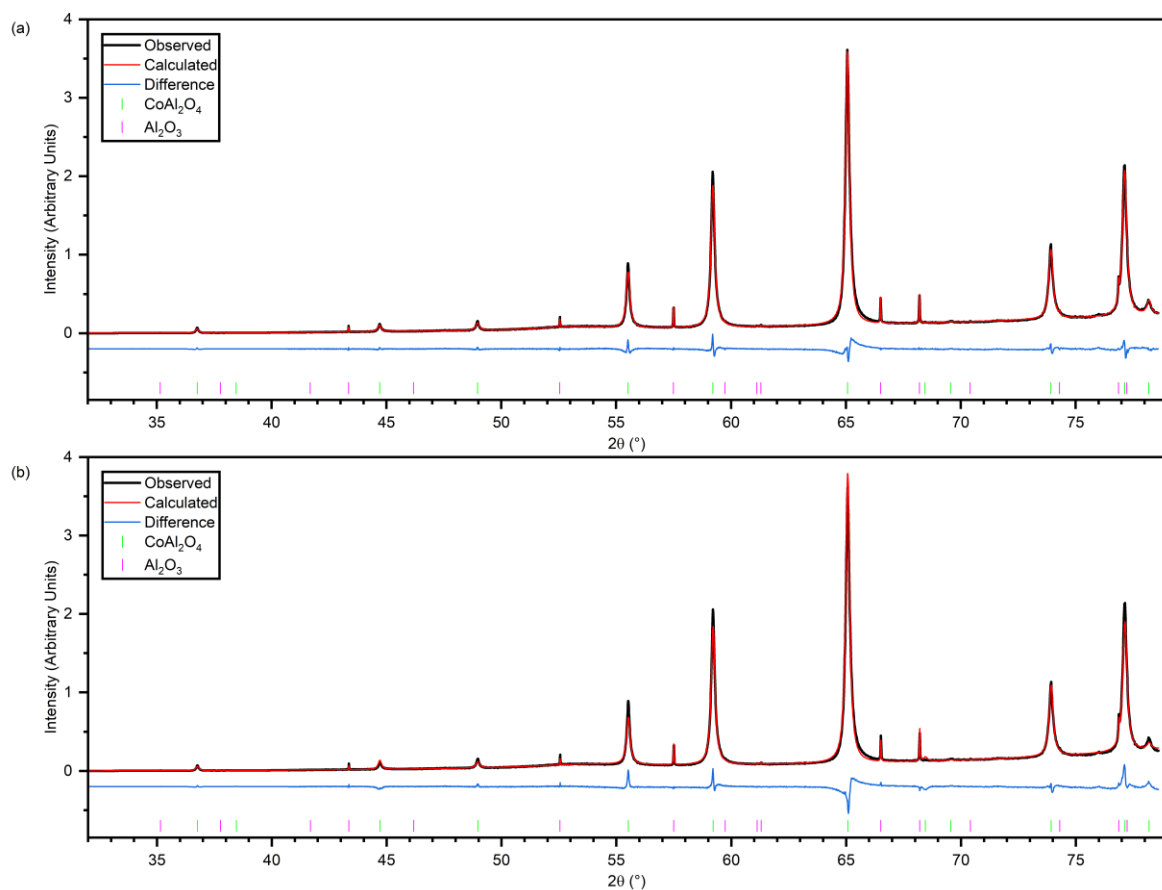


Fig. S13. (a) Pawley and (b) Rietveld fits to the Cobalt Blue diffraction pattern. In each case the difference plot is shown offset on the vertical scale. Similar to Cerulean Blue, Cobalt Blue contains a spinel and weak diffraction peaks attributed to Al_2O_3 . The lattice parameter of the spinel is consistent with that of CoAl_2O_4 (Table S5). A Rietveld refinement (Fig. S13b) was carried out in order to determine phase fractions.

Ultramarine Blue (Michael Harding No. 113)

Table S6. Refined crystallographic parameters for the identified phase in Ultramarine Blue.

	Literature	Pawley Fit
Lazurite ($P\bar{4}3n$)	ICSD Code 49759 ^a	
a (Å)	9.105 (2)	9.07944 (12)
Crystallite size (nm)		25.5 (3)
R_{wp} (%)		5.60

^aFormula $\text{Na}_{8.56}(\text{Al}_6\text{Si}_6\text{O}_{24})(\text{SO}_4)_{1.56}\text{S}_{0.44}$.

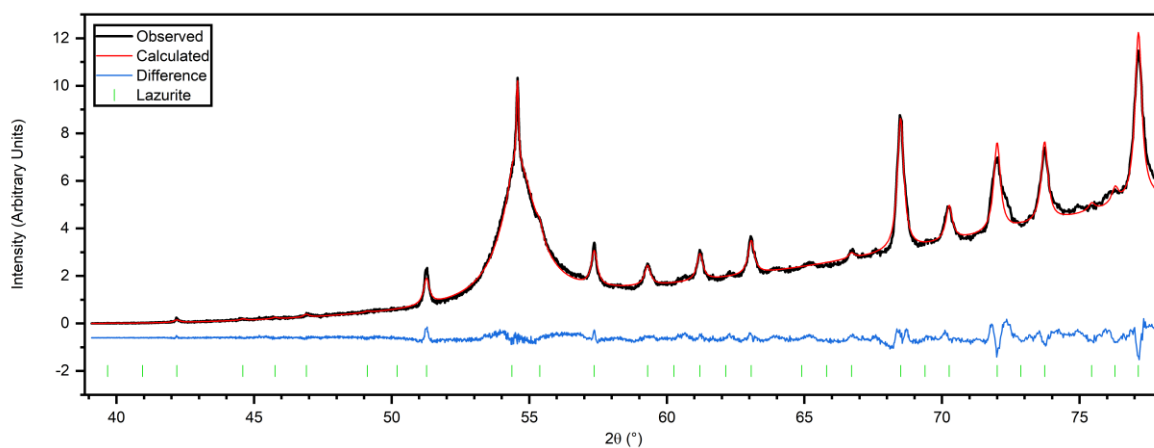


Fig. S14. Pawley fit to the Ultramarine Blue diffraction pattern. The difference plot is shown offset on the vertical scale. The broad peak centred on $2\theta = 54.8^\circ$ is due to diffraction by the graphitic vacuum window, and was fitted by inclusion of two pseudo-Voigt functions.

The diffraction pattern is consistent with the presence of a sodalite framework structure adopted by lazurite (Fig. S14, Table S6). The structure-type accommodates a wide range of compositional variety and the data were insufficient to allow a full structural model to be constructed.

Manganese Violet (Michael Harding No. 304)

Table S7. Refined crystallographic parameters for the identified phases in Manganese Violet.

	Literature	Pawley Fit	Rietveld Fit
α-NH₄MnP₂O₇ (<i>P2₁/c</i>)	Begum and Wright [4]		
<i>a</i> (Å)	7.4252 (3)	7.4150 (2)	7.4147 (3)
<i>b</i> (Å)	9.6990 (4)	9.7047 (3)	9.7049 (3)
<i>c</i> (Å)	8.6552 (4)	8.6451 (3)	8.6457 (3)
β (°)	105.627 (3)	105.551 (2)	105.545 (3)
Crystallite size (nm)		102 (3)	111 (5)
Weight fraction (%)	69 (3)		71 (2)
β-NH₄MnP₂O₇ (<i>P1</i>)	Begum and Wright [4]		
<i>a</i> (Å)	8.4034 (6)	8.40359 (14)	8.4036 (2)
<i>b</i> (Å)	6.1498 (4)	6.14997 (5)	6.1497 (2)
<i>c</i> (Å)	6.1071 (4)	6.10641 (6)	6.1064 (2)
α (°)	104.618 (5)	104.6288 (11)	104.620 (3)
β (°)	100.748 (5)	100.7411 (10)	100.743 (3)
γ (°)	96.802 (6)	96.8044 (11)	96.808 (3)
Crystallite size (nm)		480 (40)	300 (35)
Weight fraction (%)	31 (3)		29 ^a (2)
<i>R_{wp}</i> (%)		11.3	33.1

^aThis phase has poor powder averaging.

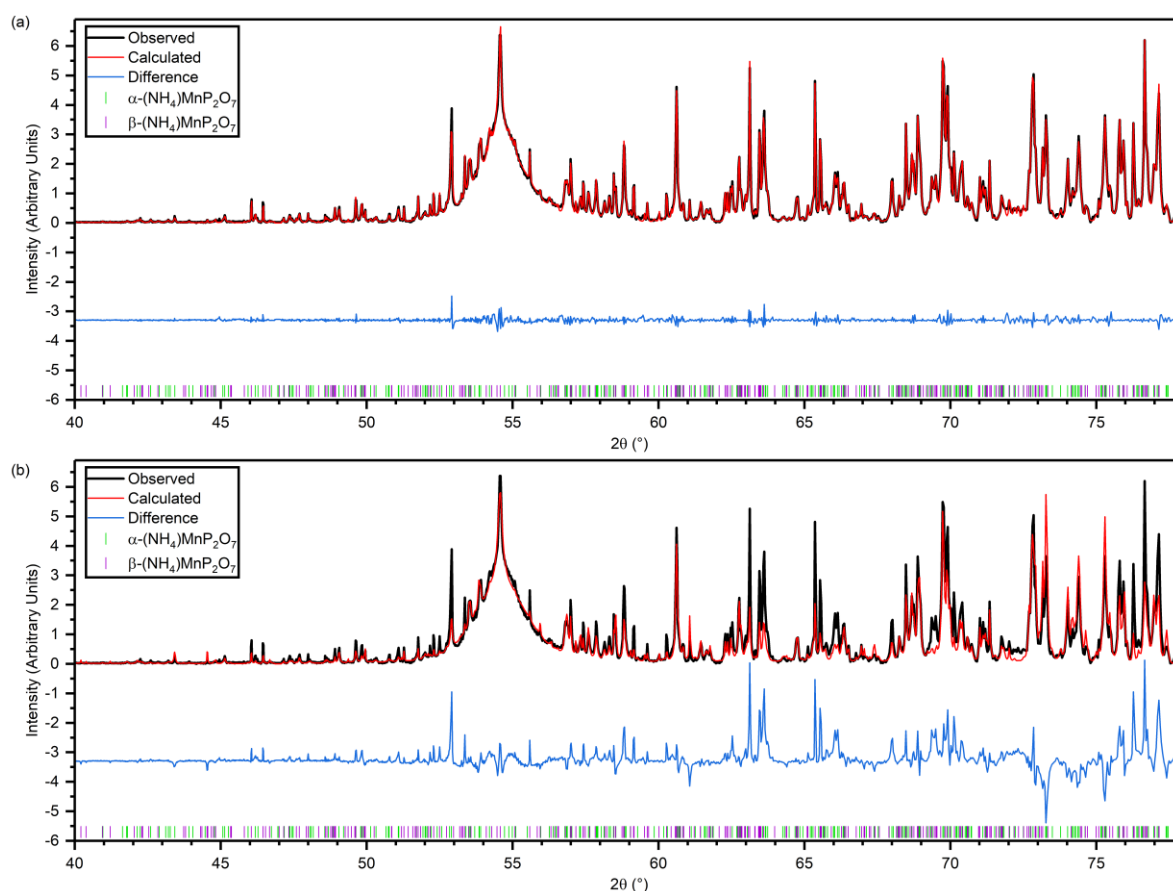


Fig. S15. (a) Pawley and (b) Rietveld fits to the Manganese Violet diffraction pattern. In each case the difference plot is shown offset on the vertical scale. The broad peak centred on $2\theta = 54.8^\circ$ is due to diffraction by the graphitic vacuum window, and was fitted by inclusion of two pseudo-Voigt functions.

The Rietveld refinement provides a significantly poorer fit than the Pawley fit (Fig. S15), demonstrated by the larger R_{wp} value (Table S7). This is mostly due to poor powder averaging of the β - $\text{NH}_4\text{MnP}_2\text{O}_7$ phase which is likely to reduce the accuracy of the phase quantification but it is assumed that the large number of peaks aids in ‘averaging out’ any errors. The analysis of this paint is described in more detail in the main article.

Chrome Oxide Green (Michael Harding No. 305)

Table S8. Refined crystallographic parameters for the identified phase in Chrome Oxide Green.

	Literature	Pawley Fit
Cr_2O_3 ($R\bar{3}c$)	ICSD Code 75577	
a (Å)	4.9570 (3)	4.95905 (1)
c (Å)	13.5923 (2)	13.59696 (3)
Crystallite size (nm)		70.6 (2)
R_{wp} (%)		8.11

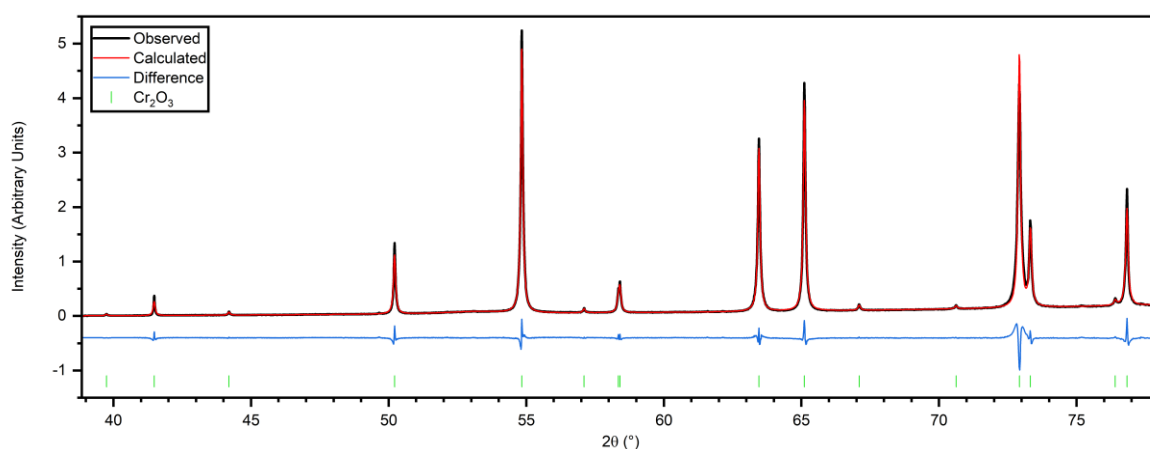


Fig. S16. Pawley fit to the Chrome Oxide Green diffraction pattern. The difference plot is shown offset on the vertical scale.

All diffraction peaks can be indexed to a corundum-type cell (Fig. S16) consistent with Cr_2O_3 , with a mean crystallite size of 70.6 (2) nm (Table S8).

Cobalt Turquoise (Michael Harding No. 507)

Table 9. Refined crystallographic parameters for the identified phases in Cobalt Turquoise.

	Literature	Pawley Fit ^a	
CoCr_2O_4 ($Fd\bar{3}m$)	ICSD Code 61612		
a (Å)	8.3346 (3)	8.32044 (1)	8.32992 (3)
Crystallite size (nm)		72.5 (2)	
Cr_2O_3 ($R\bar{3}c$)	ICSD Code 75577		
a (Å)	4.9570 (3)	4.9522 (2)	4.95764 (15)
c (Å)	13.5923 (2)	13.5663 (7)	13.5910 (7)
Crystallite size (nm)		79 (3)	
R_{wp} (%)		4.77	

^aTwo distinct compositions were observed for each phase.

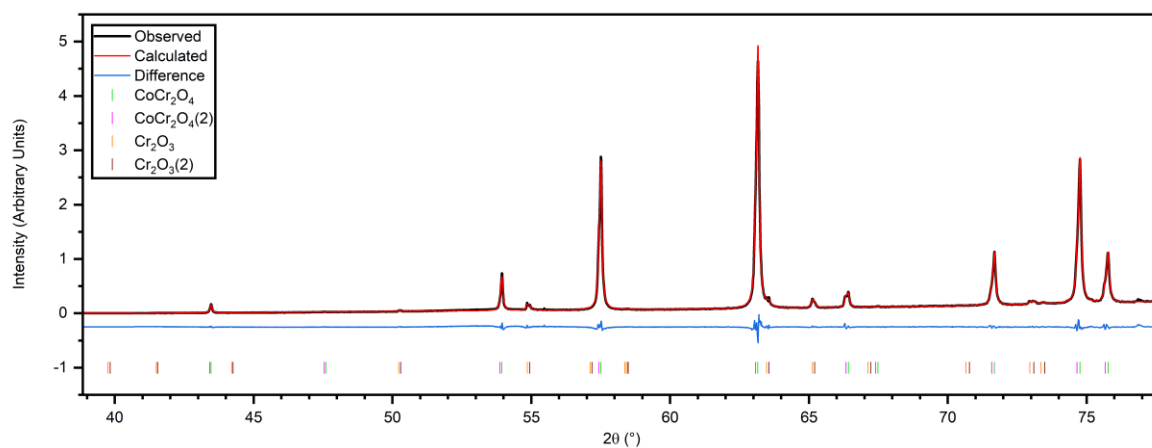


Fig. S17. Pawley fit to the Cobalt Turquoise diffraction pattern. The difference plot is shown offset on the vertical scale.

The diffraction pattern of this paint contains peaks attributable to the spinel CoCr_2O_4 and to Cr_2O_3 (Fig. S17). However, close study of the pattern reveals splitting in the peaks of both phases consistent with two distinct compositions for each phase. In order to fit this robustly, the primary and secondary compositions were constrained to have the same fitted widths (and therefore identical derived mean crystallite sizes). In both cases the second composition has cell parameters 0.1 – 0.2% smaller, indicative of a small degree of substitution by an unidentified element, most likely to be either Co or Al. It is likely that the Cr_2O_3 phase represents left-over raw material from the synthesis of the spinel and therefore that the presence of two distinct spinel phases is a direct consequence of the presence of two Cr_2O_3 phases.

Observation of the peak splitting was possible only because of the very high resolution of the technique. It may be that the bimodal characteristic of these phases is restricted to one supplier and perhaps for a limited period of time, offering an additional potential method to distinguish otherwise similar paints for the purposes of authentication or art history research. Similar peak splitting has also been observed for the crystalline phases in Lemon Yellow and Aureolin.

Chrome Green (Rublev Colours)

Table S10. Refined crystallographic parameters for the identified phase in Chrome Green.

	Literature	Pawley Fit
$\text{PbCr}_{1-x}\text{S}_x\text{O}_4$ (<i>Pnma</i>)	Monico <i>et al.</i> [5] ^a	
<i>a</i> (Å)	8.592 (2)	8.585 (3)
<i>b</i> (Å)	5.527 (2)	5.514 (2)
<i>c</i> (Å)	7.061 (2)	7.069 (2)
Crystallite size (nm)		8.5 (7)
<i>R_{wp}</i> (%)		6.59

^a*x* = 0.2.

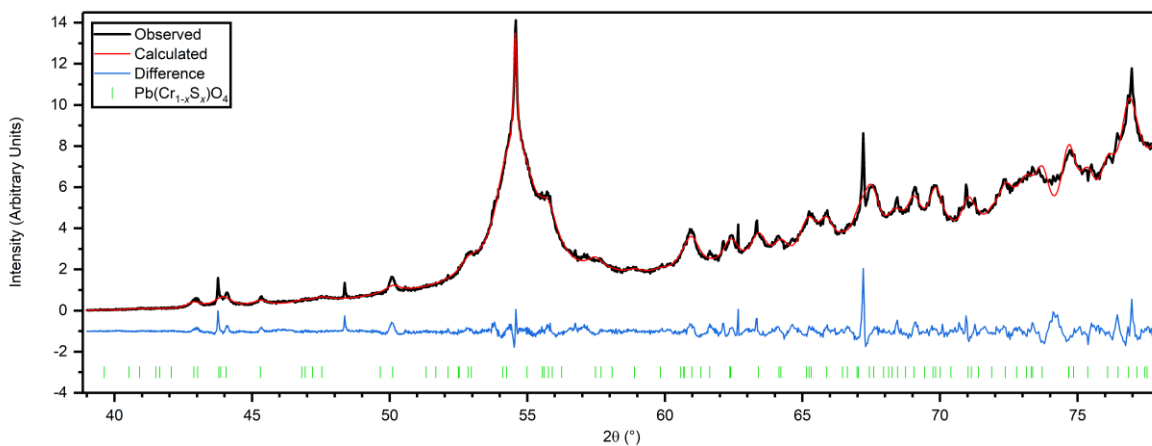


Fig. S18. Pawley fit to the Chrome Green diffraction pattern. The difference plot is shown offset on the vertical scale. The broad peak centred on $2\theta = 54.8^\circ$ is due to diffraction by the graphitic vacuum window, and was fitted by inclusion of two pseudo-Voigt functions.

According to the supplier, the Chrome Green paint contains a mixture of the pigments chrome yellow (lead chromate, PbCrO_4) and Prussian blue (ferric ferrocyanide, $\text{Fe}_4[\text{Fe}(\text{CN})_6]_3 \cdot x\text{H}_2\text{O}$). The Chrome Green diffraction pattern can be fitted with an orthorhombic phase corresponding to $\text{PbCr}_{1-x}\text{S}_x\text{O}_4$. The fitted unit cell dimensions are close to those reported by Monico *et al* [5] for $x = 0.2$, though slightly smaller which indicates marginally greater S content (Table S10). $\text{PbCr}_{1-x}\text{S}_x\text{O}_4$ occurs in both monoclinic and orthorhombic forms; the latter has a miscibility gap from $x = 0.2$ to 0.9 and is metastable with respect to the monoclinic phase for low values of x [6].

Some unidentified sharp diffraction peaks with poor powder averaging can be seen at $2\theta = 43.8^\circ$, 48.4° , 62.7° , 67.2° , 70.9° and 77.0° (Fig. S18). These peaks do not correspond to the positions expected for Prussian blue.

Lemon Yellow (Michael Harding No. 108)

Table S11. Refined crystallographic parameters for the identified phase in Lemon Yellow.

	Literature	Pawley Fit
BaCrO₄ (<i>Pnma</i>)	ICSD Code 62560	
<i>a</i> (Å)	9.113 (4)	9.11019 (2)
<i>b</i> (Å)	5.528 (3)	5.53102 (2)
<i>c</i> (Å)	7.336 (4)	7.33603 (2)
Crystallite size (nm)		159.5 (8)
<i>R_{wp}</i> (%)		9.66

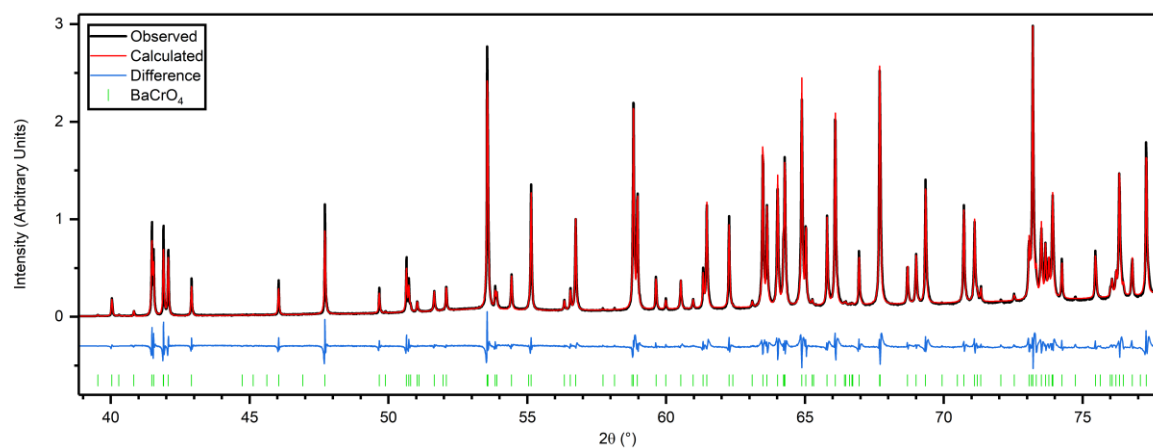


Fig. S19. Pawley fit to the Lemon Yellow diffraction pattern. The difference plot is shown offset on the vertical scale.

The only crystalline phase observed in Lemon Yellow was BaCrO₄ (Table S11). A small shoulder on the high angle side of each diffraction peak was noted (Fig. S19). This peak asymmetry is likely to be caused by a second phase of slightly different composition.

Aureolin (Michael Harding No. 501)

Table S12. Refined crystallographic parameters for the identified phases in Aureolin.

	Literature	Pawley Fit ^b	
K₃[Co(NO₂)₆] (<i>Fm</i>$\bar{3}$)	Vendilo <i>et al.</i> [7] ^a		
<i>a</i> (Å)	10.468 (6) – 10.498 (7)	10.4861 (5)	10.4953 (4)
Crystallite size (nm)		61 (2)	
<i>R</i> _{wp} (%)		6.71	

^aMultiple compositions reported.

^bTwo distinct compositions observed.

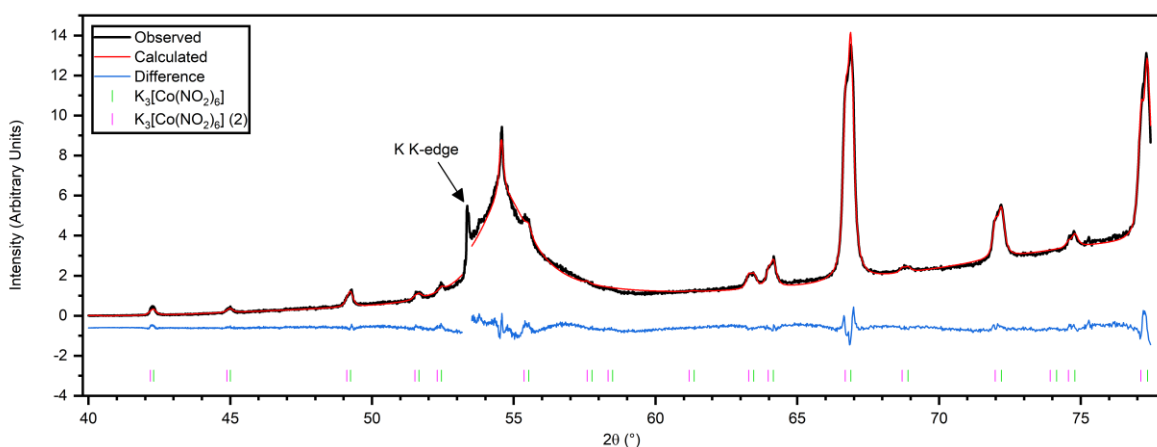


Fig. S20. Pawley fit to the Aureolin diffraction pattern. The difference plot is shown offset on the vertical scale. The broad peak centred on $2\theta = 54.8^\circ$ is due to diffraction by the graphitic vacuum window, and was fitted by inclusion of two pseudo-Voigt functions. The diffraction pattern included a strong K K-edge at $2\theta = 53.3^\circ$ that was difficult to remove due to its proximity to the vacuum window diffraction feature. This region was excluded from the fit.

Aureolin can be fitted by two K₃[Co(NO₂)₆] phases with lattice parameters 10.4953 (4) Å and 10.4861 (5) Å (Table S12). The lattice parameters fall within the range reported by Vendilo *et al.* [7] who suggested that varying amounts of Na and H₂O were responsible for the differing lattice

parameters. Due to the heavy overlap of peaks the crystallite size of both phases was constrained to be the same.

Chrome Yellow (Rublev Colours)

Table S13. Refined crystallographic parameters for the identified phases in Chrome Yellow.

	Literature	Pawley Fit	Rietveld Fit
PbCrO₄ (<i>P2₁/n</i>) ICSD Code 40920			
<i>a</i> (Å)	7.127 (2)	7.1216 (2)	7.1233 (3)
<i>b</i> (Å)	7.438 (2)	7.4335 (2)	7.4336 (3)
<i>c</i> (Å)	6.799 (2)	6.7996 (2)	6.8006 (2)
β (°)	102.43 (2)	102.434 (3)	102.448 (4)
Crystallite size (nm)		64.0 (11)	69 (2)
Weight fraction (%)			94 (1)
BaSO₄ (<i>Pnma</i>) ICSD Code 200112			
<i>a</i> (Å)	8.8842 (12)	8.8691 (6)	8.873 (3)
<i>b</i> (Å)	5.4559 (8)	5.4511 (5)	5.455 (2)
<i>c</i> (Å)	7.1569 (9)	7.1504 (4)	7.152 (3)
Crystallite size (nm)		90 (6)	64 (19)
Weight fraction (%)			6 (1)
<i>R_{wp}</i> (%)		8.19	17.8

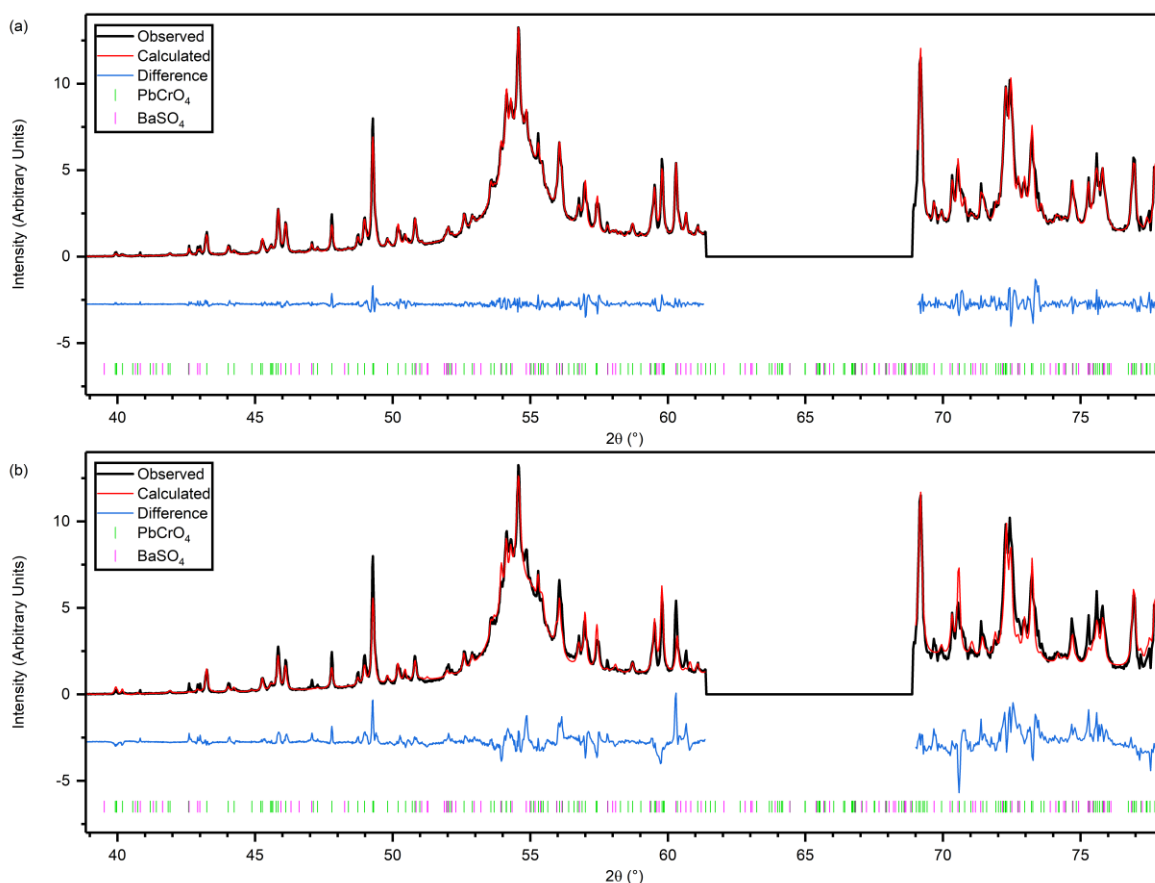


Fig. S21. (a) Pawley and (b) Rietveld fits to the Chrome Yellow diffraction pattern. In each case the difference plot is shown offset on the vertical scale. The broad peak centred on $2\theta = 54.8^\circ$ is due to diffraction by the graphitic vacuum window, and was fitted by inclusion of two pseudo-Voigt functions.

A data acquisition error meant that no data was collected in the range $61.4^\circ < 2\theta < 68.9^\circ$ (Fig. S21). The phases present, PbCrO_4 and BaSO_4 (Table S13), could be readily identified despite the missing data.

Vermilion (Rublev Colours)

Table S14. Refined crystallographic parameters for the identified phase in Vermilion.

	Literature	Pawley Fit
HgS ($P3_221$)	ICSD Code 70054	
a (Å)	4.145 (2)	4.14883 (7)
c (Å)	9.496 (2)	9.4970 (4)
Crystallite size (nm)		16.91 (10)
R_{wp} (%)		7.43

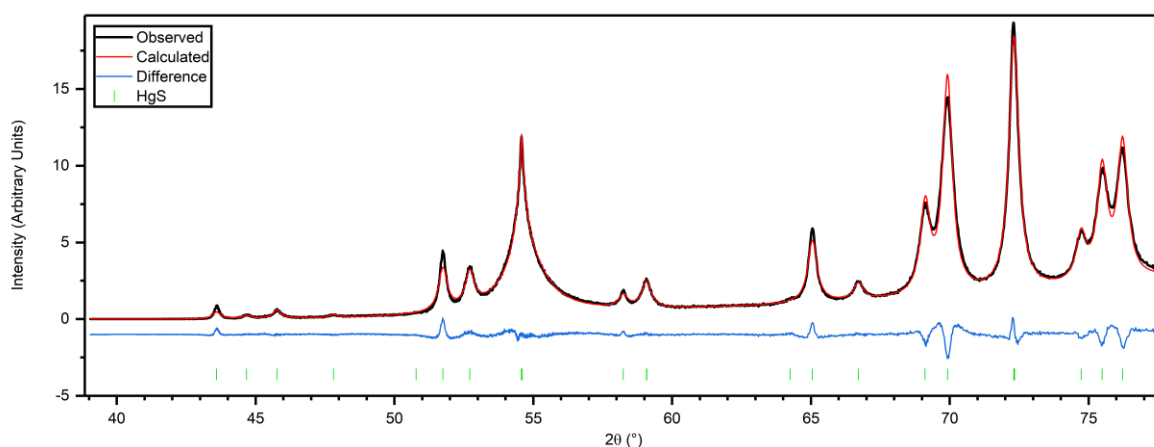


Fig. S22. Pawley fit to the Vermilion diffraction pattern. The difference plot is shown offset on the vertical scale. The broad peak centred on $2\theta = 54.8^\circ$ is due to diffraction by the graphitic vacuum window, and was fitted by inclusion of two pseudo-Voigt functions.

HgS (cinnabar) can be fitted to the Vermilion diffraction pattern (Fig. S22). Analysis of the significant peak broadening suggests a crystallite size of 16.91 (10) nm (Table S14).

Minium (Rublev Colours)

Table S15. Refined crystallographic parameters for the identified phase in Minium.

	Literature	Pawley Fit
Pb₃O₄ ($P4_2/mbc$)	ICSD Code 4106	
a (Å)	8.811 ^a	8.81596 (3)
c (Å)	6.563 ^a	6.56641 (2)
R_{wp} (%)		5.59

^aError estimates not reported.

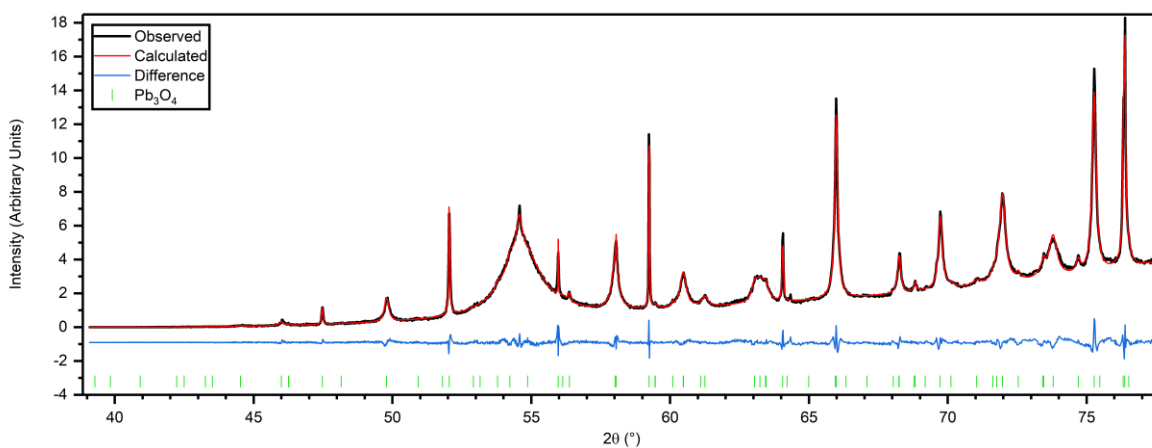


Fig. S23. Pawley fit to the Minium diffraction pattern. The difference plot is shown offset on the vertical scale. The broad peak centred on $2\theta = 54.8^\circ$ is due to diffraction by the graphitic vacuum window, and was fitted by inclusion of two pseudo-Voigt functions.

All the peaks of the Minium paint diffraction pattern can be attributed to a single Pb_3O_4 phase (which has the mineral name minium). The pattern exhibits extremely anisotropic peak broadening (Fig. S23). An anisotropic crystallite size model [8] did not satisfactorily fit the pattern, with the largest improvement given by the Stephens anisotropic strain model [9]. For comparison, the R_{wp} values for an isotropic peak shape, an anisotropic crystallite size model and an anisotropic strain model were 12.4%, 9.82% and 5.59% (Table S15) respectively. This result is consistent with previous studies [10] and it appears that microstrain anisotropy is an inherent property of the crystal structure.

French Yellow Ochre (Michael Harding No. 133)

Table S16. Refined crystallographic parameters for the identified phases in French Yellow Ochre.

	Literature	Pawley Fit
$\alpha\text{-FeOOH}$ (goethite) ($Pbnm$)	ICSD Code 239324	
a (Å)	4.6145 (8)	4.5977 (4)
b (Å)	9.9553 (17)	9.9215 (11)
c (Å)	3.0177 (5)	3.0087 (4)
Crystallite size (nm)		17.9 (4)
SiO_2 (quartz) ($P3_221$)	ICSD Code 34644	
a (Å)	4.9138 (2)	4.91511 (2)
c (Å)	5.4052 (2)	5.40583 (3)
Crystallite size (nm)		126 (2)
TiO_2 (rutile) ($P4_2/mnm$)	ICSD Code 9161	
a (Å)	4.5941 (1)	4.5939 (2)
c (Å)	2.9589 (1)	2.9589 (3)
Crystallite size (nm)		141 (23)
R_{wp} (%)		9.76

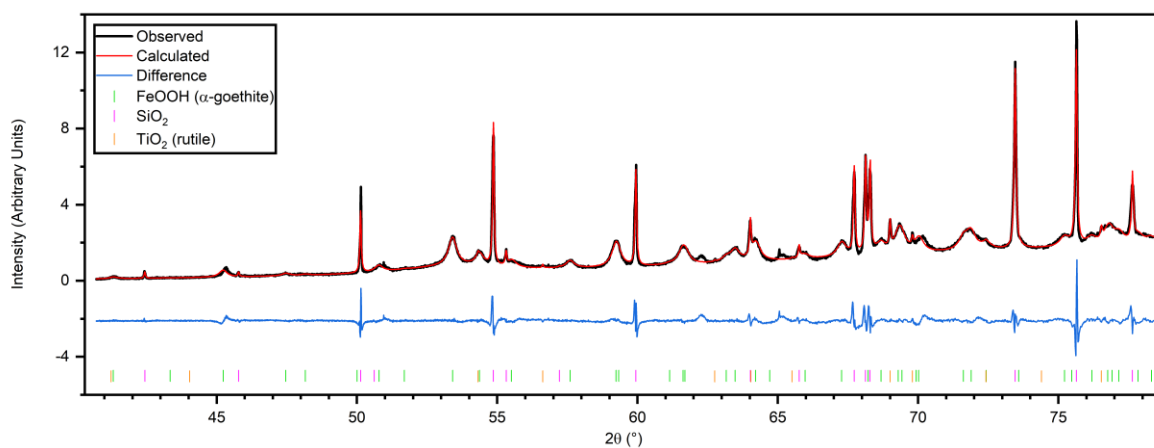


Fig. S24. Pawley fit to the French Yellow Ochre diffraction pattern. The difference plot is shown offset on the vertical scale.

A Pawley fit to the diffraction pattern of French Yellow Ochre (Fig. S24) based on α -FeOOH (goethite), SiO₂ (quartz) and TiO₂ (rutile) accounts for the majority of peaks, with weak unidentified peaks at $2\theta = 62.3^\circ$ and 65.2° . Goethite was found to have small crystallites of mean diameter 17.9 (4) nm, whilst the quartz and rutile phases have much sharper peaks (Table S16). These two phases also show extremely poorly powder averaging and consequently no Rietveld fit was attempted.

Raw Sienna (Michael Harding No. 120)

Table S17. Refined crystallographic parameters for the identified phases in Raw Sienna.

	Literature	Pawley Fit
α-FeOOH (goethite) (<i>Pbnm</i>)		
	ICSD Code 239324	
<i>a</i> (Å)	4.6145 (8)	4.6094 (4)
<i>b</i> (Å)	9.9553 (17)	9.9639 (11)
<i>c</i> (Å)	3.0177 (5)	3.0207 (2)
Crystallite size (nm)		13.3 (2)
SiO₂ (quartz) (<i>P3₂21</i>)		
	ICSD Code 34644	
<i>a</i> (Å)	4.9138 (2)	4.9144 (2)
<i>c</i> (Å)	5.4052 (2)	5.4050 (15)
Crystallite size (nm)		130 (20)
TiO₂ (rutile) (<i>P4₂/mnm</i>)		
	ICSD Code 9161	
<i>a</i> (Å)	4.5941 (1)	4.5872 (2)
<i>c</i> (Å)	2.9589 (1)	2.95790 (7)
Crystallite size (nm)		220 (30)
<i>R</i> _{wp} (%)		5.68

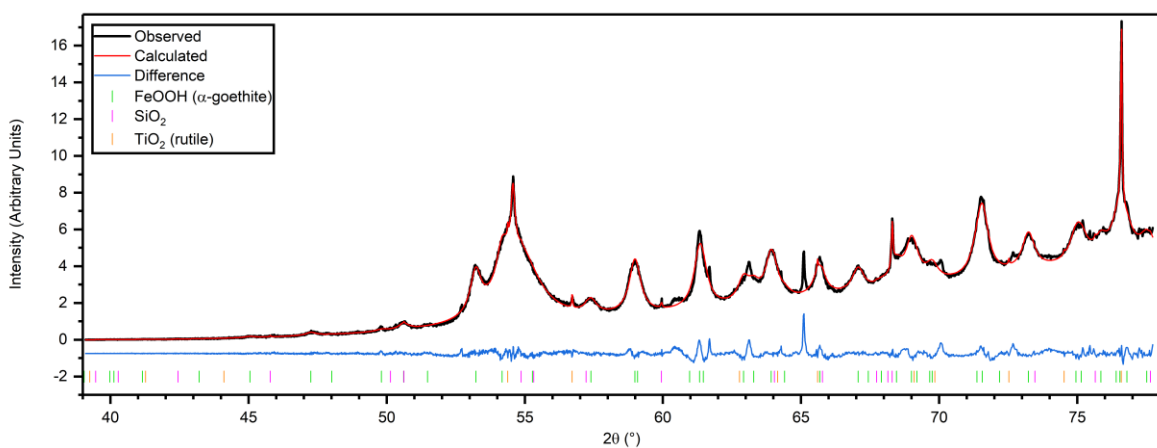


Fig. S25. Pawley fit to the Raw Sienna diffraction pattern. The difference plot is shown offset on the vertical scale. The broad peak centred on $2\theta = 54.8^\circ$ is due to diffraction by the graphitic vacuum window, and was fitted by inclusion of two pseudo-Voigt functions.

Raw Sienna is composed mostly of goethite, with several peaks attributed to quartz and rutile though several expected peaks for these phases have no appreciable intensity due to poor powder-averaging (Fig. S25). The goethite mean crystallite size is 13.3 (2) nm (Table S17), similar to the size found in French Yellow Ochre (and Raw Umber, below). Several diffraction peaks remain unidentified.

Raw Umber (Michael Harding No. 121)

Table S18. Refined crystallographic parameters for the identified phases in Raw Umber.

	Literature	Pawley Fit
α-FeOOH (goethite) (<i>Pbnm</i>)	ICSD Code 239324	
<i>a</i> (Å)	4.6145 (8)	4.6016 (12)
<i>b</i> (Å)	9.9553 (17)	9.969 (2)
<i>c</i> (Å)	3.0177 (5)	3.0105 (4)
Crystallite size (nm)		6.51 (13)
SiO₂ (quartz) (<i>P3₂21</i>)	ICSD Code 34644	
<i>a</i> (Å)	4.9138 (2)	4.91479 (12)
<i>c</i> (Å)	5.4052 (2)	5.40545 (15)
Crystallite size (nm)		410 (60)
R_{wp} (%)		4.06

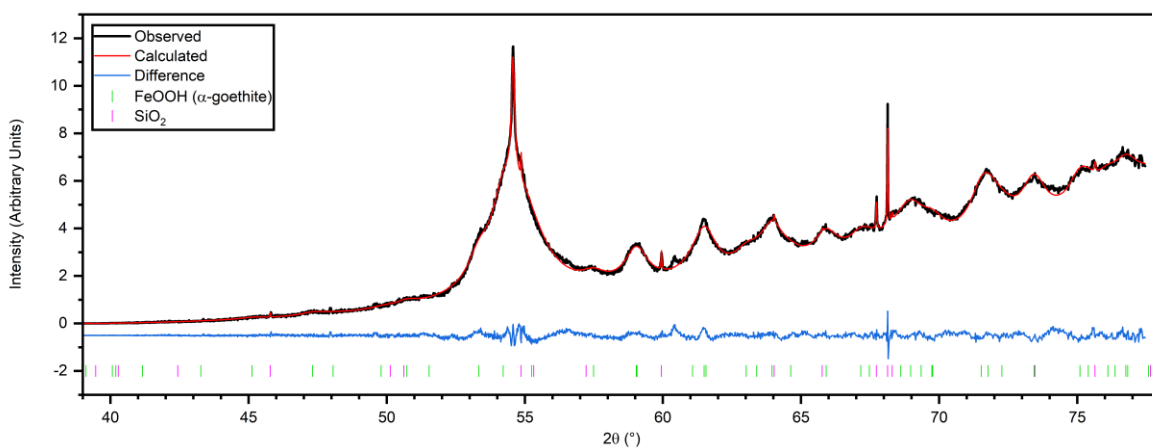


Figure S26. Pawley fit to the Raw Umber diffraction pattern. The difference plot is shown offset on the vertical scale. The broad peak centred on $2\theta = 54.8^\circ$ is due to diffraction by the graphitic vacuum window, and was fitted by inclusion of two pseudo-Voigt functions.

As for French Yellow Ochre and Raw Sienna, Raw Umber consists mainly of goethite (Fig. S26) and poorly powder-averaged quartz, though no rutile peaks were observed in this case. The goethite peaks were exceptionally broad, yielding a crystallite size of 6.51 (13) nm (Table S18).

Transparent Red Oxide (Michael Harding No. 220)

Table S19. Refined crystallographic parameters for the identified phase in Transparent Red Oxide.

	Literature	Pawley Fit
Fe₂O₃ (hematite) (<i>R</i>$\bar{3}c$)	ICSD Code 7797	
<i>a</i> (Å)	5.0324 (9)	5.03661 (3)
<i>c</i> (Å)	13.7643 (4)	13.7606 (4)
<i>L_x</i> (nm)		8.25 (2)
<i>L_z</i> (nm)		4.36 (2)
<i>R_{wp}</i> (%)		3.13

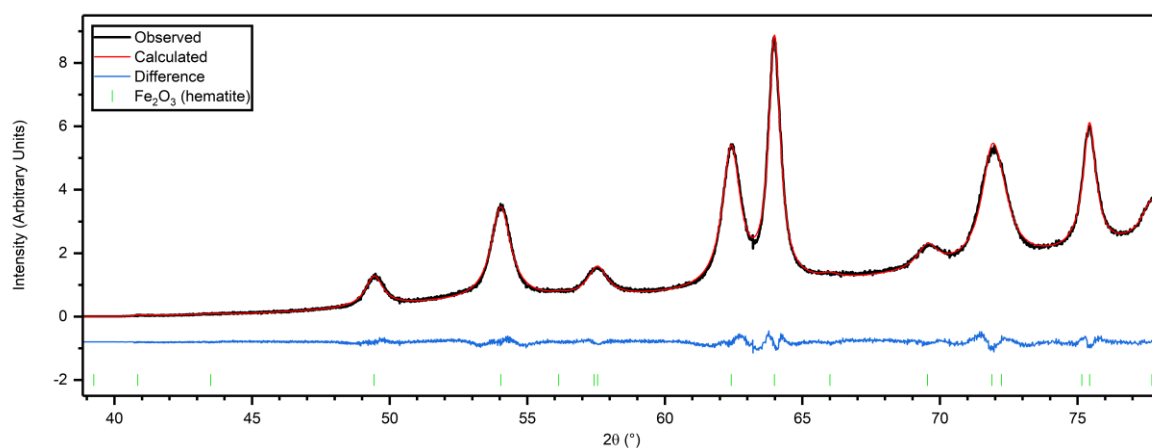


Fig. S27. Pawley fit to the Transparent Red Oxide diffraction pattern. The difference plot is shown offset on the vertical scale.

Transparent red oxide consists of Fe₂O₃ (hematite) (Fig. S27). The manufacturer notes the pigment's exceptionally small crystallite size and the diffraction peaks are broadened anisotropically. Application of the crystallite shape model of Ectors *et al* [8] suggests platy crystallites with an *L_x* : *L_z* ratio ~2 assuming cylindrical crystallites (Table S19). It should be noted however that a fit using the

Stephens anisotropic strain model [9] instead of crystallite size is of comparable quality ($R_{wp} = 2.97\%$), albeit with several additional refined parameters.

Cremnitz White (Michael Harding No. 307)

Table S20. Refined crystallographic parameters for the identified phases in Cremnitz White.

	Literature	Pawley Fit	Rietveld Fit ^a
2PbCO₃•Pb(OH)₂ ($R\bar{3}m$)	Siidra <i>et al.</i> [11]		
<i>a</i> (Å)	5.2475 (1)	5.24372 (6)	5.2442 (2)
<i>c</i> (Å)	23.6795 (7)	23.68405 (10)	23.6841 (3)
<i>L_x</i> (nm)		230 (30)	76 (8)
<i>L_z</i> (nm)		32.8 (4)	36.6 (10)
Weight fraction (%)			81.0 (8)
PbCO₃ (<i>Pmcn</i>)	Antao & Hassan [12]		
<i>a</i> (Å)	5.18324 (2)	5.18265 (5)	5.1820 (3)
<i>b</i> (Å)	8.49920 (3)	8.50094 (9)	8.5022 (4)
<i>c</i> (Å)	6.14746 (3)	6.14231 (8)	6.1424 (3)
Crystallite size (nm)		89 (2)	72 (3)
Weight fraction (%)			19.0 ^b (8)
<i>R_{wp}</i> (%)		7.2	21.0

^aPreferred orientation of the hydrocerussite phase was fitted by an eight-term spherical harmonics model.

^bThis phase has poor powder averaging.

The analysis of this paint is described in more detail in the main article.

Flake White (Michael Harding No. 703)

Table S21. Refined crystallographic parameters for the identified phases in Flake White.

	Literature	Pawley Fit	Rietveld Fit
2PbCO₃•Pb(OH)₂ ($R\bar{3}m$)	Siidra <i>et al.</i> [11]		
<i>a</i> (Å)	5.2475 (1)	5.24405 (2)	5.24403 (5)
<i>c</i> (Å)	23.6795 (7)	23.6819 (2)	23.6822 (4)
<i>L_x</i> (nm)		136 (6)	104 (6)
<i>L_z</i> (nm)		32.6 (6)	37.0 (14)
<i>r^a</i>			0.709 (6)
Weight fraction (%)			56.2 (10)
PbCO₃ (<i>Pmcn</i>)	Antao & Hassan [12]		
<i>a</i> (Å)	5.18324 (2)	5.18236 (13)	5.1834 (4)
<i>b</i> (Å)	8.49920 (3)	8.4968 (2)	8.4977 (6)
<i>c</i> (Å)	6.14746 (3)	6.1435 (2)	6.1410 (5)
Crystallite size (nm)		95 (2)	71 (5)
Weight fraction (%)			10.9 ^b (5)
ZnO (<i>P6₃mc</i>)	NIST [13]		
<i>a</i> (Å)	3.24983 (8)	3.249919 (9)	3.24992 (2)
<i>c</i> (Å)	5.2068 (1)	5.20682 (3)	5.20688 (7)
Crystallite size (nm)		268 (5)	275 (11)
Weight fraction (%)			32.9 (9)
<i>R_{wp}</i> (%)		4.69	12.1

^aMarch-Dollase factor.

^bThis phase has poor powder averaging.

The analysis of this paint is described in more detail in the main article.

Zinc White (Michael Harding No. 103)

Table S22. Refined crystallographic parameters for the identified phase in Zinc White.

	Literature	Pawley Fit
ZnO (<i>P6₃mc</i>)	NIST [13]	
<i>a</i> (Å)	3.24983 (8)	3.249957 (6)
<i>c</i> (Å)	5.2068 (1)	5.20654 (2)
Crystallite size (nm)		251 (2)
<i>R_{wp}</i> (%)		9.01

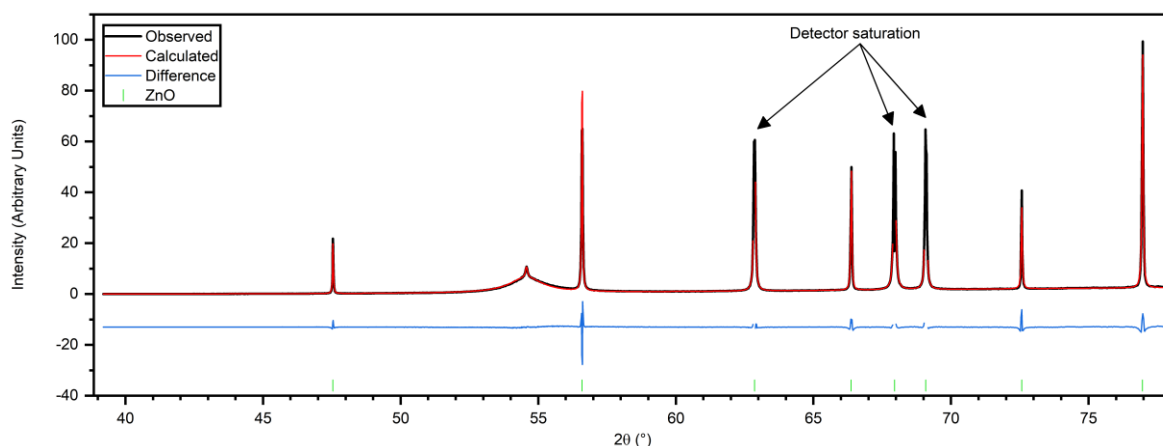


Fig. S28. Pawley fit to the Zinc White diffraction pattern. The difference plot is shown offset on the vertical scale. The broad peak centred on $2\theta = 54.8^\circ$ is due to diffraction by the graphitic vacuum window, and was fitted by inclusion of two pseudo-Voigt functions.

ZnO (zincite) was the only crystalline phase observed in Zinc White (Table S22). Several peaks in the diffraction pattern of Zinc White caused detector saturation (Fig. S28), and the affected data points were excluded from the Pawley fit.

Flemish White (Rublev Colours)

Table S23. Refined crystallographic parameters for the identified phase in Flemish White.

	Literature	Pawley Fit	Rietveld Fit
(PbO)₃PbSO₄•H₂O (<i>P1</i>)	Steele <i>et al</i> [14]		
<i>a</i> (Å)	6.3682 (2)	6.3737 (5)	6.3755 (5)
<i>b</i> (Å)	7.4539 (3)	7.4520 (7)	7.4487 (6)
<i>c</i> (Å)	10.2971 (4)	10.2987 (6)	10.2970 (7)
α (°)	75.33 (3)	75.351 (7)	75.324 (6)
β (°)	79.40 (1)	79.413 (7)	79.416 (7)
γ (°)	88.34 (1)	88.228 (8)	88.267 (7)
Crystallite size (nm)		42.5 (16)	39.9 (13)
<i>R_{wp}</i> (%)		3.63	12.0

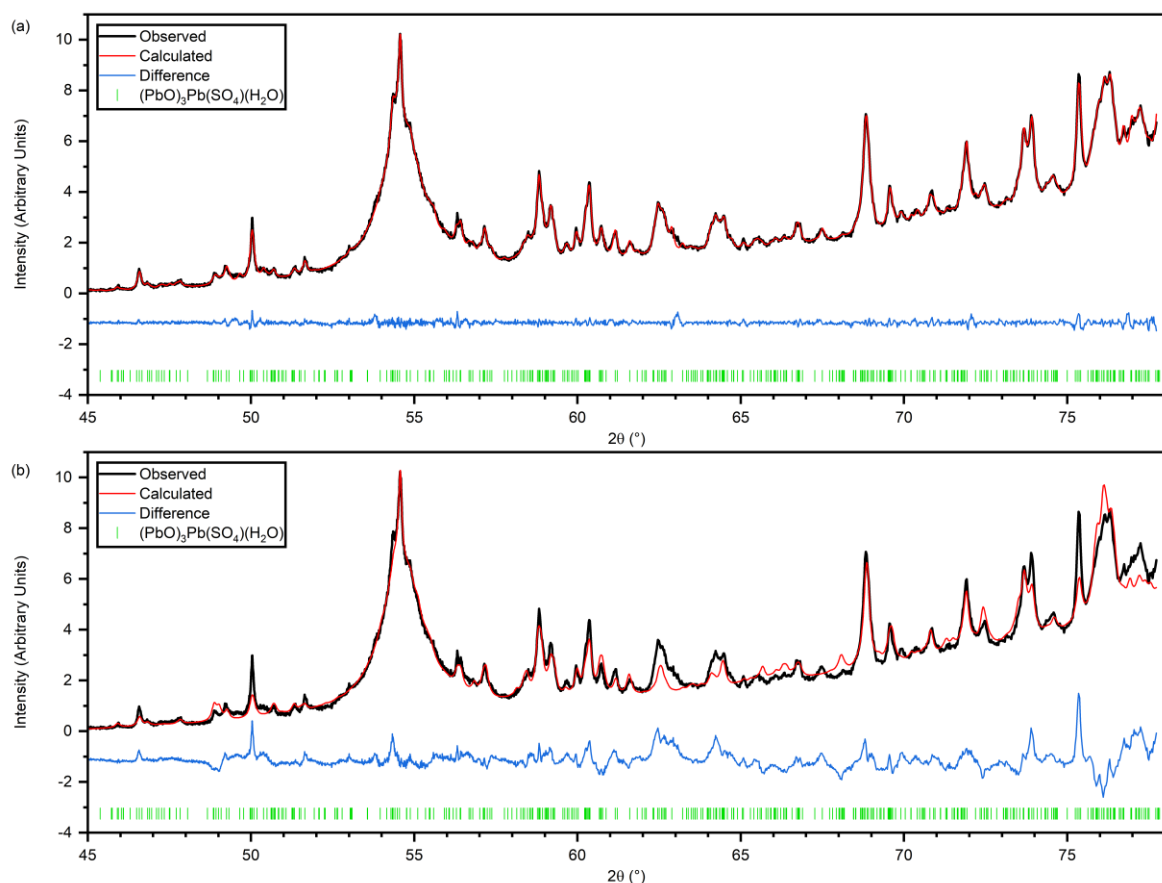


Fig. S29. (a) Pawley and (b) Rietveld fits to the Flemish White diffraction pattern. In each case the difference plot is shown offset on the vertical scale. The broad peak centred on $2\theta = 54.8^\circ$ is due to diffraction by the graphitic vacuum window, and was fitted by inclusion of two pseudo-Voigt functions.

A Pawley fit to Flemish White based on $(\text{PbO})_3\text{PbSO}_4 \cdot \text{H}_2\text{O}$ yields a good fit (Fig. S29a). However, the high density of allowed reflections means that a good agreement from a Pawley fit does not necessarily guarantee the correct structure has been assigned. To test whether the phase assignment is correct, a Rietveld refinement was carried out (Fig. S29b) in which the unit cell parameters were allowed to vary but the structural model was fixed to that of Steele *et al* [14]. The relative peak intensities are reproduced sufficiently well to provide convincing confirmation of the assignment.

Titanium White No. 3 (Michael Harding No. 130)

Table S24. Refined crystallographic parameters for the identified phases in Titanium White No. 3.

	Literature	Pawley Fit	Rietveld Fit
TiO₂ (rutile) (<i>P4₂/mnm</i>)	ICSD Code 9161		
<i>a</i> (Å)	4.5941 (1)	4.593985 (10)	4.59391 (3)
<i>c</i> (Å)	2.9589 (1)	2.958962 (10)	2.95900 (2)
Crystallite size (nm)		130.6 (6)	122.9 (13)
Weight fraction (%)			71.5 (6)
ZnO (<i>P6₃mc</i>)	NIST [13]		
<i>a</i> (Å)	3.24983 (8)	3.249915 (6)	3.249855 (14)
<i>c</i> (Å)	5.2068 (1)	5.206793 (16)	5.20688 (3)
Crystallite size (nm)		192.6 (12)	188 (3)
Weight fraction (%)			28.5 (6)
<i>R_{wp}</i> (%)		6.49	14.6

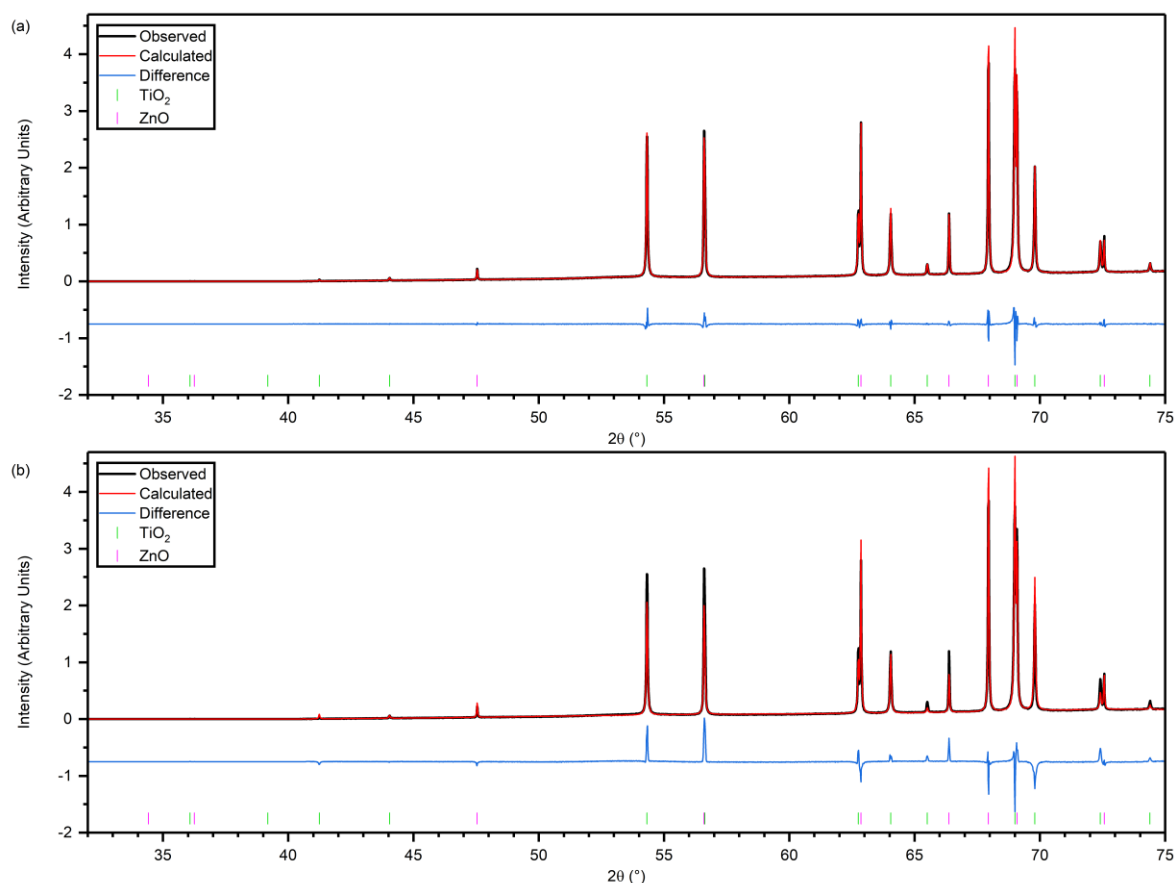


Fig. S30. (a) Pawley and (b) Rietveld fits to the Titanium White No. 3 diffraction pattern. In each case the difference plot is shown offset on the vertical scale.

Titanium White No. 3 paint was found to contain both TiO_2 (rutile) and ZnO (Fig. S30) in approximately a 2.5 : 1 ratio (Table S24).

Ivory Black (Michael Harding No. 129)

Table S25. Refined crystallographic parameters for the identified phases in Ivory Black.

	Literature	Pawley Fit	Rietveld Fit
$\text{Ca}_5(\text{PO}_4)_3\text{OH}$ ($P6_3/m$)	ICSD Code 56307		
a (Å)	9.4249 (4)	9.4244 (5)	9.4236 (4)
c (Å)	6.8838 (4)	6.8848 (4)	6.8850 (4)
Crystallite size (nm)		18.7 (12)	21.9 (12)
Weight fraction (%)			81.2 (13)
CaCO_3 ($R\bar{3}c$)	ICSD Code 18166		
a (Å)	4.9900 (2)	4.9833 (5)	4.9835 (7)
c (Å)	17.002 (1)	17.059 (2)	17.059 (3)
Crystallite size (nm)		29 (2)	22.1 (13)
Weight fraction (%)			18.8 (13)
R_{wp} (%)		3.99	5.44

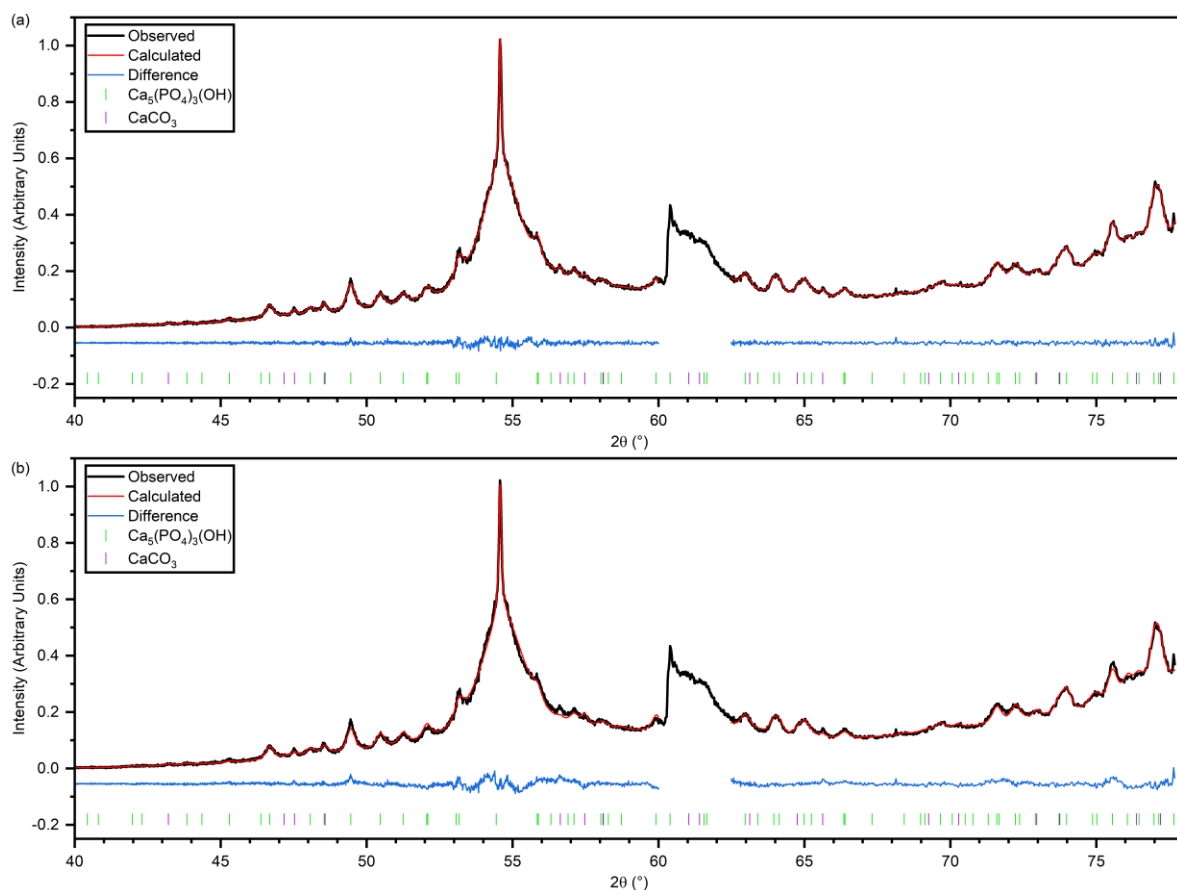


Fig. S31. (a) Pawley and (b) Rietveld fits to the Ivory Black diffraction pattern. In each case the difference plot is shown offset on the vertical scale. The broad peak centred on $2\theta = 54.8^\circ$ is due to diffraction by the graphitic vacuum window, and was fitted by inclusion of two pseudo-Voigt functions.

The diffraction pattern of Ivory Black can be fitted with $\text{Ca}_5(\text{PO}_4)_3\text{OH}$ (hydroxyapatite) and CaCO_3 (calcite) (Table S25). A strong Ca K-edge is seen at $2\theta = 60.3^\circ$ (Fig. S31). The edge and XAFS region were excluded from the fits. The black colour of the paint is expected to be due to carbonaceous material that is probably amorphous and is therefore undetected in this experiment. Strictly speaking, this paint does not meet the group A definition – that the pigment itself has been detected using XRD. However, the pigment is derived from burnt bone (according to the supplier) and the hydroxyapatite phase, and probably the calcite also, is therefore intimately linked with the carbonaceous material.

7.2 Group B Paints

Manganese Blue (BLOCKX)

Table S26. Refined crystallographic parameters for the identified phase in Manganese Blue.

	Literature	Pawley Fit
ZnO (<i>P6₃mc</i>)	NIST [13]	
<i>a</i> (Å)	3.24983 (8)	3.249900 (3)
<i>c</i> (Å)	5.2068 (1)	5.206880 (9)
Crystallite size (nm)		150.7 (4)
<i>R_{wp}</i> (%)		7.08

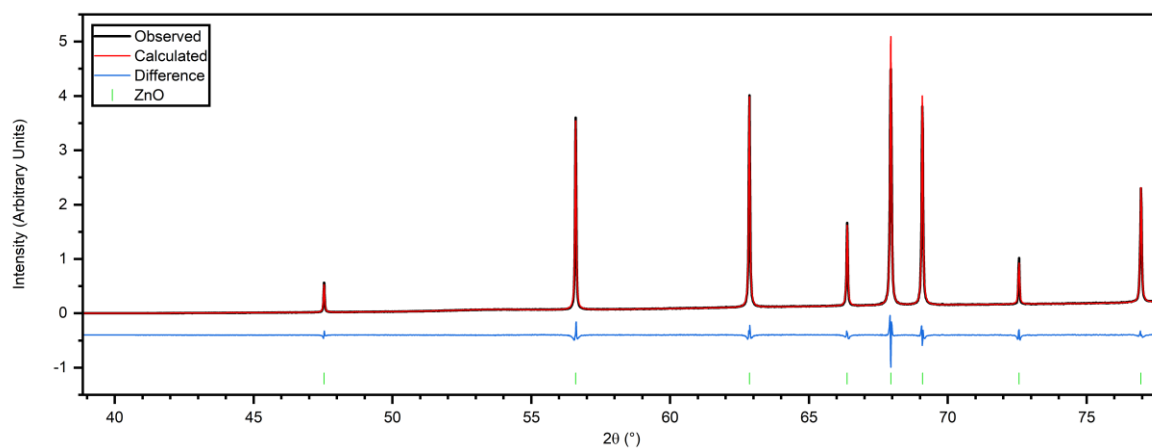


Fig. S32. Pawley fit to the Manganese Blue diffraction pattern. The difference plot is shown offset on the vertical scale.

ZnO was the only crystalline phase observed in Manganese Blue. The pigment in this paint is specified as phthalocyanine blue by the supplier.

Dioxazine Violet (BLOCKX)

Table S27. Refined crystallographic parameters for the identified phase in Dioxazine Violet.

	Literature	Pawley Fit
CaCO₃ (<i>R</i>$\bar{3}$<i>c</i>)	ICSD Code 18166	
<i>a</i> (Å)	4.9900 (2)	4.98237 (8)
<i>c</i> (Å)	17.002 (1)	17.0237 (3)
Crystallite size (nm)		53.8 (9)
<i>R</i> _{wp} (%)		3.80

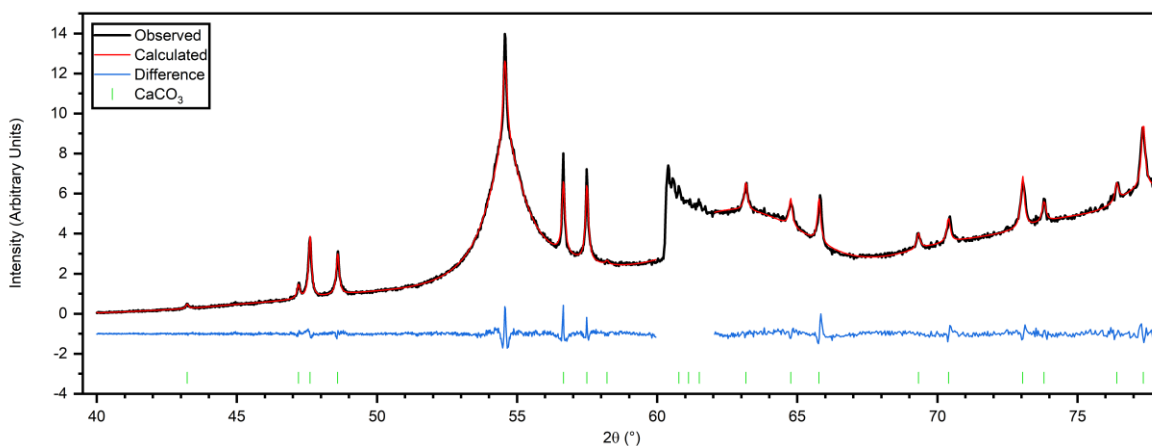


Fig. S33. Pawley fit to the Dioxazine Violet diffraction pattern. The difference plot is shown offset on the vertical scale. The broad peak centred on $2\theta = 54.8^\circ$ is due to diffraction by the graphitic vacuum window, and was fitted by inclusion of two pseudo-Voigt functions.

CaCO₃ (calcite) was the only crystalline phase observed in Dioxazine Violet. A strong Ca K-edge is seen at $2\theta = 60.3^\circ$ (Fig. S33). The edge and XAFS region were excluded from the Pawley fit. The pigment in this paint is specified as dioxazine by the supplier.

Bright Yellow Lake (Michael Harding No. 109)

Table S28. Refined crystallographic parameters for the identified phase in Bright Yellow Lake.

	Literature	Pawley Fit
TiO₂ (rutile) (<i>P4₂/mnm</i>)	ICSD Code 9161	
<i>a</i> (Å)	4.5941 (1)	4.59370 (5)
<i>c</i> (Å)	2.9589 (1)	2.95854 (6)
Crystallite size (nm)		143 (4)
<i>R_{wp}</i> (%)		3.51

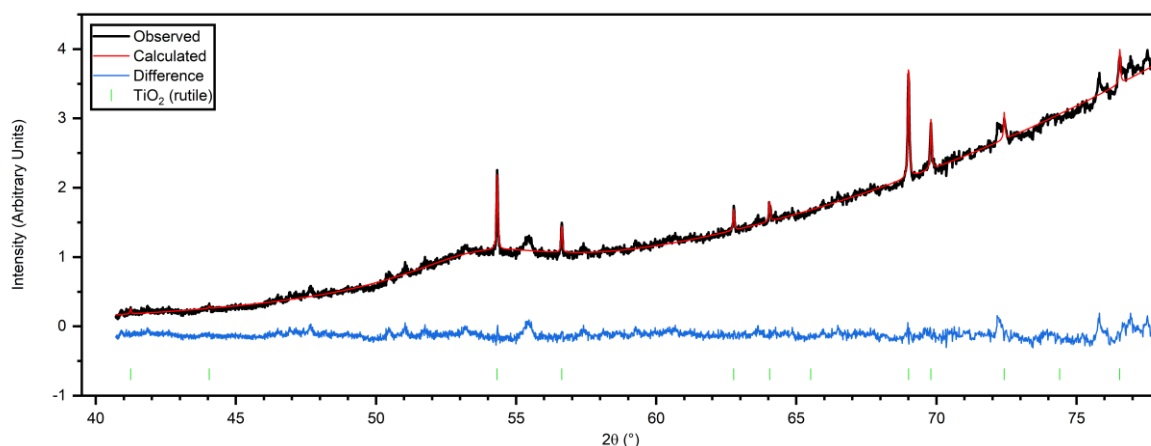


Fig. S34. Pawley fit to the Bright Yellow Lake diffraction pattern. The difference plot is shown offset on the vertical scale.

Rutile was the only phase identified in Bright Yellow Lake. However, several weak, relatively broad diffraction peaks remain unidentified. The pigment in this paint is specified as an arylamide (PY3) by the supplier.

Pyrrolo-Vermilion (BLOCKX)

Table S29. Refined crystallographic parameters for the identified phases in Pyrrolo-Vermilion.

	Literature	Pawley Fit
CaCO₃ (<i>R3c</i>)	ICSD Code 18166	
<i>a</i> (Å)	4.9900 (2)	4.98072 (5)
<i>c</i> (Å)	17.002 (1)	17.02445 (9)
Crystallite size (nm)		76.0 (15)
TiO₂ (rutile) (<i>P4₂/mnm</i>)	ICSD Code 9161	
<i>a</i> (Å)	4.5941 (1)	4.59387 (2)
<i>c</i> (Å)	2.9589 (1)	2.95881 (3)
Crystallite size (nm)		130 (2)
<i>R_{wp}</i> (%)		9.67

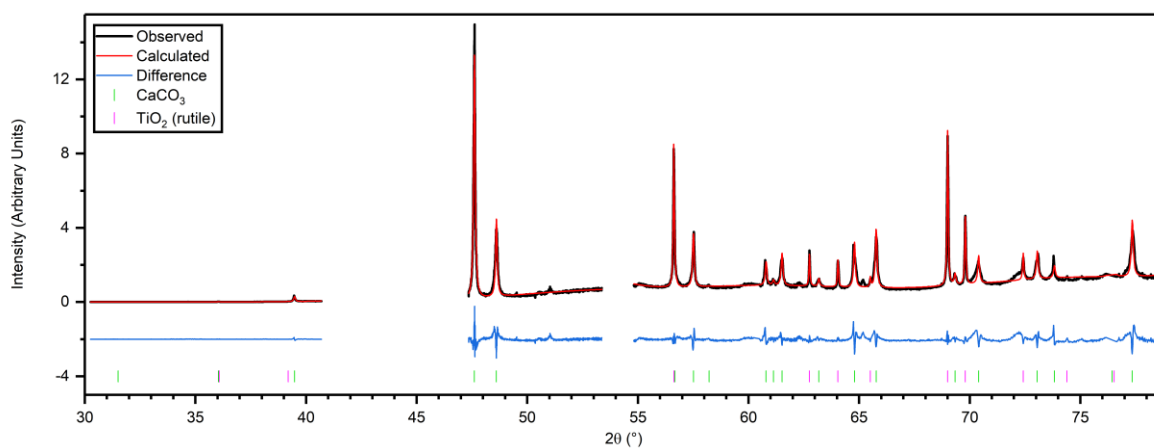


Fig. S35. Pawley fit to the Pyrrolo-Vermilion diffraction pattern. The difference plot is shown offset on the vertical scale.

Two segments of the data in the ranges $40.7^{\circ} \leq 2\theta \leq 47.3^{\circ}$ and $53.4^{\circ} \leq 2\theta \leq 54.8^{\circ}$ were corrupted at the data acquisition stage and were excluded from the fit (Fig. S35). The diffraction pattern shows that Pyrrolo-Vermilion contains CaCO_3 (calcite) and TiO_2 (rutile). As for Bright Yellow Lake, there are several weak unidentified diffraction peaks. The pigment in this paint is specified as pyrrolo orange (PO73) by the supplier.

7.3 Group C Paints

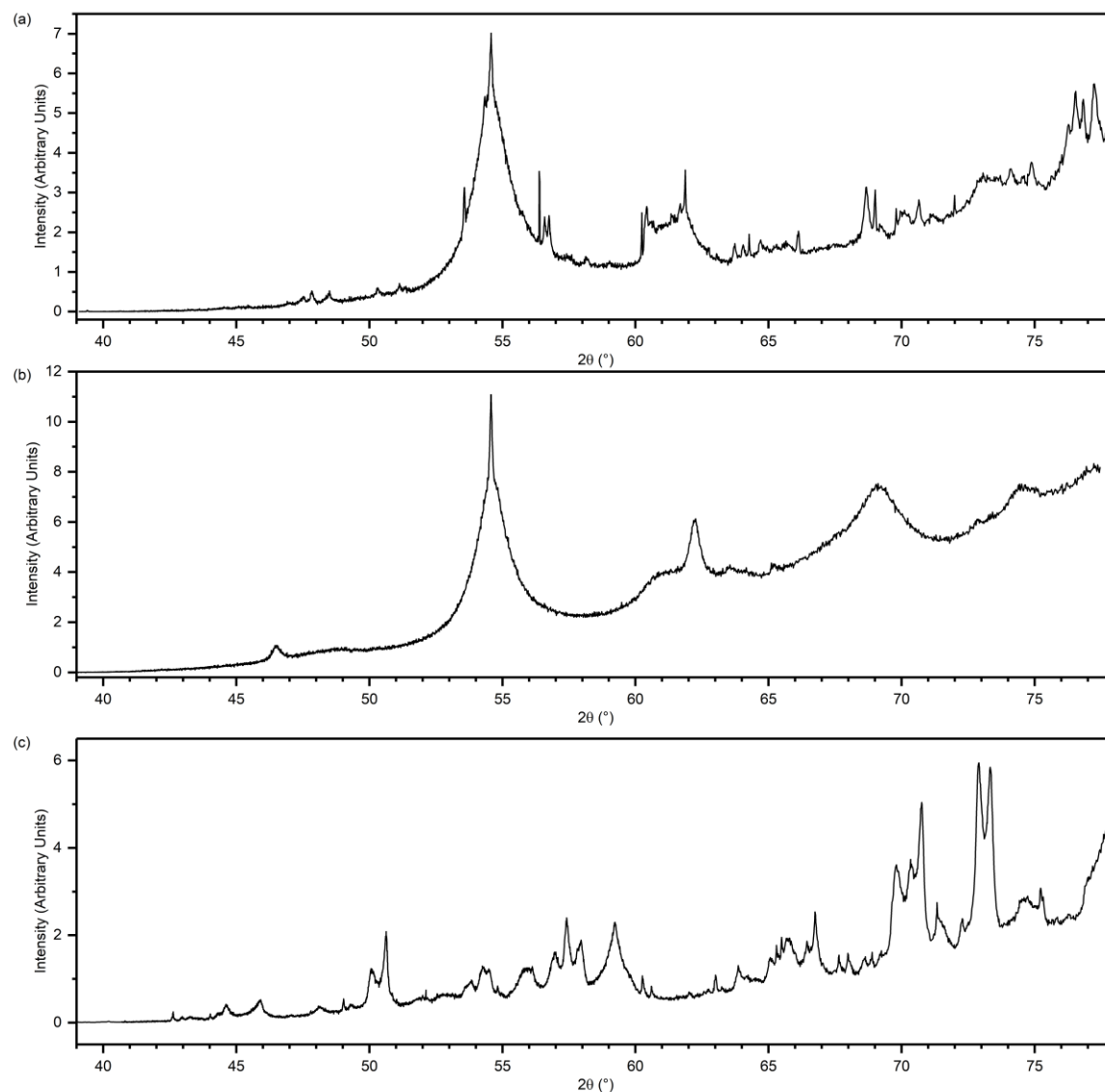


Fig. S36. Diffraction patterns of the Group C paints. (a) Terre Vert (Michael Harding No. 115), (b) Viridian (BLOCKX) and (c) Orange Molybdate (Rublev Colours). The broad peak centred on $2\theta = 54.8^\circ$ in (a) and (b) is due to diffraction by the graphitic vacuum window. The Terre Vert pattern (a) has a Ca-K absorption edge at $2\theta = 60.3^\circ$.

Although the Group C paints have obvious diffraction peaks (Fig. S36), no phases have been identified. Terre Vert contains the ‘green earth’ pigment (PG23) and there are therefore a relatively large number of candidate phases, and there may also be a complex mixture present. Orange Molybdate is expected to contain lead chromate molybdate (PR104). However, attempts to fit the pattern with the appropriate phase candidates were unsuccessful. The Viridian pattern shows a small number of broad, though variable-width, diffraction peaks. The peak positions do not correspond to those predicted for a range of plausible candidate phases. As noted in Section 3 of the main article, the pigment is expected to be $\text{Cr}_2\text{O}_3 \cdot 2\text{H}_2\text{O}$ but there are no published crystal structures for this phase. It seems likely that the pattern recorded in this work contains structural information but it is not interpretable without, for example, reference to structural models that attempt to explain the lack of long-range crystallinity.

7.4 Group D Paints

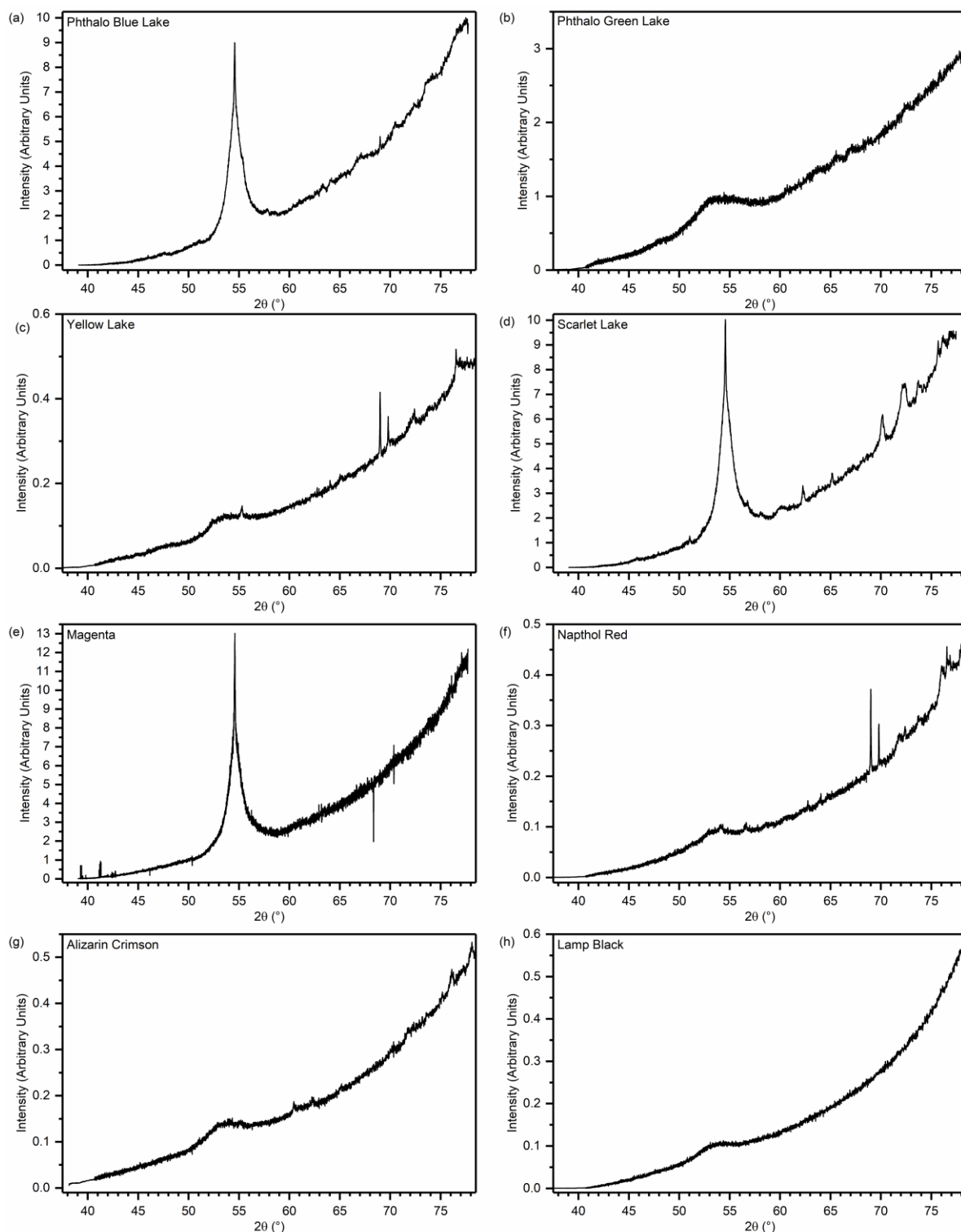


Fig. S37. Diffraction patterns of the Group D paints. (a) Phthalo Blue Lake (Michael Harding No. 209), (b) Phthalo Green Lake (Michael Harding No. 213), (c) Yellow Lake (Michael Harding No. 110), (d) Scarlet Lake (Michael Harding No. 205), (e) Magenta (Michael Harding No. 303), (f) Naphthol Red (Michael Harding No. 301), (g) Alizarin Crimson (Michael Harding No. 302), (h) Lamp Black (Michael Harding No. 128). (a), (d) and (e) contain a broad peak centred on $2\theta = 54.8^\circ$ that is due to diffraction by the graphitic vacuum window. (c) and (f) contain diffraction peaks from TiO_2 , rutile ($2\theta = 69.0^\circ$, 69.8°) and a Ti K-edge at $2\theta = 76.2^\circ$, believed to be due to ‘break-through’ of the white paint layer on the canvas beneath the paint samples.

Of the group D paints, only the diffraction patterns of Magenta and Lamp Black are truly devoid of any diffraction peaks (excluding the vacuum window peaks). The very sharp features in the Magenta pattern are noise peaks. It is assumed that the observed diffraction peaks, other than the rutile peaks, are due to the synthetic organic pigments that are expected to be present in these paints (except Lamp Black). For example, it is possible to do a Pawley fit of the Scarlet Lake pattern using a published crystal structure of naphthol (PR170). However, organic pigments typically have low crystal symmetry and relatively large unit cells leading to a very high density of diffraction peaks in the 2θ range observed. Together with the low-quality observed diffraction patterns, it is not possible to uniquely identify the pigments present or to extract meaningful crystallographic parameters using an assumed crystal structure.

8. References

- [1] G. M. Hansford, S. M. R. Turner, P. Degryse, A. J. Shortland, High-resolution X-ray diffraction with no sample preparation, *Acta Cryst. A* 73 (2017) 293-311.
- [2] A. Polak, T. Kelman, P. Murray, S. Marshall, D. J. M. Stothard, N. Eastaugh, F. Eastaugh, Hyperspectral imaging combined with data classification techniques as an aid for artwork authentication, *J. Cult. Herit.* 26 (2017) 1-11.
- [3] L. Verger, O. Dargaud, G. Rousse, E. Rozsályi, A. Juhin, D. Cabaret, M. Cotte, P. Glatzel, L. Cormier, Spectroscopic properties of Cr^{3+} in the spinel solid solution $\text{ZnAl}_{2-x}\text{Cr}_x\text{O}_4$, *Phys. Chem. Minerals* 43 (2016) 33-42.
- [4] Y. Begum, A. J. Wright, Relating highly distorted Jahn–Teller MnO_6 to colouration in manganese violet pigments, *J. Mater. Chem.* 22 (2012) 21110-21116.
- [5] L. Monico, K. Janssens, C. Miliani, B. G. Brunetti, M. Vagnini, F. Vanmeert, G. Falkenberg, A. Abakumov, Y. Lu, H. Tian, J. Verbeeck, M. Radepon, M. Cotte, E. Hendriks, M. Geldof, L. van der Loeff, J. Salvant, M. Menu, Degradation Process of Lead Chromate in Paintings by Vincent van Gogh Studied by Means of Spectromicroscopic Methods. 3. Synthesis, Characterization, and Detection of Different Crystal Forms of the Chrome Yellow Pigment, *Anal. Chem.* 85 (2013) 851-859.
- [6] M. J. Crane, P. Leverett, L. R. Shaddick, P. A. Williams, J. T. Klopogge, R. L. Frost, The PbCrO_4 - PbSO_4 system and its mineralogical significance, *N. Jb. Miner. Mh.* 11 (2001) 505-519.
- [7] A. G. Vendilo, N. E. Kovaleva, V. I. Chistov, V. M. Retivov, Potassium cobaltinitrite, *Russ. J. Inorg. Chem.* 56 (2011) 501-505.
- [8] D. Ectors, F. Goetz-Neunhoffer, J. Neubauer, A generalized geometric approach to anisotropic peak broadening due to domain morphology, *J. Appl. Cryst.* 48 (2015) 189-194.
- [9] P. Stephens, Phenomenological model of anisotropic peak broadening in powder diffraction, *J. Appl. Cryst.* 32 (1999) 281-289.
- [10] A. Leineweber, R. E. Dinnebier, Anisotropic microstrain broadening of minium, Pb_3O_4 , in a high-pressure cell: interpretation of line-width parameters in terms of stress variations, *J. Appl. Cryst.* 43 (2010) 17-26.
- [11] O. Siidra, D. Nekrasova, W. Depmeier, N. Chukanov, A. Zaitsev, R. Turner, Hydrocerussite-related minerals and materials: structural principles, chemical variations and infrared spectroscopy, *Acta Cryst. B* 74 (2018) 182-195.
- [12] S.M. Antao, I. Hassan, The Orthorhombic Structure of CaCO_3 , SrCO_3 , PbCO_3 And BaCO_3 : Linear Structural Trends, *Can. Mineral.* 47 (2009) 1245-1255.
- [13] National Institute of Standards and Technology, Standard Reference Material 1979: Powder Diffraction Line Profile Standard for Crystallite Size Analysis (Nano-Crystalline Zinc Oxide Powder), 2016. Available at: <https://www-s.nist.gov/srmors/certificates/1979.pdf>
- [14] I. M. Steele, J. J. Pluth, J. W. Richardson Jr., *J. Solid State Chem.* 132 (1997) 173-181.